MODEL-INDEPENDENT MEASUREMENT OF THE EXCITED FRACTION IN A MAGNETO-OPTICAL TRAP(MOT)

by

MUDESSAR H. SHAH

M. Phil., Quaid-I-Azam University-Pakistan 1998

AN ABSTRACT OF A DISSERTATION

submitted in partial fulfillment of the
requirements for the degree

DOCTOR OF PHILOSOPHY

Department of Physics
College of Arts and Sciences

KANSAS STATE UNIVERSITY
Manhattan, Kansas
2006

ABSTRACT

In many experiments involving a magneto-optical trap (MOT) it is of great importance to know the fraction of atoms left in an excited state due to the trapping process. Generally speaking, researchers have had to use overly simplistic and untested models to estimate this fraction. In this work, the excited fraction of ^{87}Rb atoms in a MOT is measured using a model-free approach. A simple model is fit to the fractions which were obtained for a range of MOT parameters. Using the results of this work, the excited fraction of ^{87}Rb atoms trapped in a MOT can be accurately estimated with knowledge of only the trapping laser intensity and detuning. The results are only weakly dependent on other MOT parameters.

MODEL-INDEPENDENT MEASUREMENT OF THE EXCITED FRACTION IN A MAGNETO-OPTICAL TRAP(MOT)

by

MUDESSAR H. SHAH

M. Phil., QUAID-I-AZAM University-Pakistan, 1998

A DISSERTATION

submitted in partial fulfillment of the
requirements for the degree

DOCTOR OF PHILOSOPHY

Department of Physics
College of Arts and Sciences

KANSAS STATE UNIVERSITY
Manhattan, Kansas
2006

Approved by:

Major Professor
B. D. DePaola

ABSTRACT

In many experiments involving a magneto-optical trap (MOT) it is of great importance to know the fraction of atoms left in an excited state due to the trapping process. Generally speaking, researchers have had to use overly simplistic and untested models to estimate this fraction. In this work, the excited fraction of ^{87}Rb atoms in a MOT is measured using a model-free approach. A simple model is fit to the fractions which were obtained for a range of MOT parameters. Using the results of this work, the excited fraction of ^{87}Rb atoms trapped in a MOT can be accurately estimated with knowledge of only the trapping laser intensity and detuning. The results are only weakly dependent on other MOT parameters.

TABLE OF CONTENTS

LIST OF FIGURES

LIST OF TABLES

DEDICATION

To my Mom and Dad.
Banaya jinkee mohabat nay nukta dan mujhko

Chapter 1

Introduction

Over the course of last two decades, much progress has been seen in the areas of BEC[1], quantum degenerate gases, precision spectroscopy[2–5], cold and ultra-cold collisions[6] and related areas. The common basis of all these fields is laser cooling and trapping of neutral atoms and ions[7,8]. Manipulating atoms with coherent light is opening new avenues for research on a regular basis.

In laser cooling and trapping, generally, an atom's translational energy is controlled by changing the internal energy of the system[9]. This leaves the atomic system in a mixture of ground and excited states. The apparatus commonly used for the cooling and trapping of atoms is called a magneto optical trap, or (MOT). A magneto optical trap[10] can take on various configurations but the most commonly used one consists of six circularly polarized beams interacting with a group of atoms. A sourceless inhomogeneous B-field is applied, localizing the atoms in a particular point in space where the field has almost zero effect.

In nearly all experiments related to cold atoms, the quantities that need to be known include total number of trapped atoms, number density and excited fraction. For instance, in the case of BEC and quantum degenerate gases, knowledge of total number of atoms is crucial. For photo-association[11–13], cold collisions[6,12], photo-ionization cross section measurements[14], and reaction chemistry[15], knowledge of excited fraction and density helps in determining the collision rates between the excited atoms. In the case of cold plasmas

excited fraction ionization rates are used as a diagnostic of plasma dynamics[16].

In many of these experiments, one way of determining total number of atoms[17] is to use the expression

$$N = \frac{N_{exc}}{f}. \tag{1.1}$$

The total number of excited atoms N_{exc}, is determined by measuring the fluorescence, the signal which depends on the location of the detector, the amplifier characteristics and many other experimental parameters. The excited fraction f is usually determined using a simple formula[18]

$$f = \frac{I/I_s}{1 + I/I_s + (2\delta/\Gamma)^2}, \tag{1.2}$$

with a known value of total intensity I, and detuning δ of the trapping laser from the transition frequency; Γ represents the full width of the transition, and I_s is the constant to be discussed later. Equation 1.2 describes a simple two level system of a low density sample of atoms, interacting with a single low intensity laser beam.

Realizing that a MOT is a more complex environment than the simple model describes, Townsend[19] proposed a modification to the two level formula that *may be* more suitable for calculating the excited fraction in a MOT. Another study, by Javanainen[20], on multilevel atoms interacting with polarized, detuned lasers led him to propose an ansatz for f.

Now the questions are "How good are these models" and "Can these models be tested by a model-independent measurement"?

In the present work we try to answer these questions by directly measuring the excited fraction in a MOT. The measuring technique we use is called MOTRIMS (magneto-optical trap recoil ion momentum spectroscopy)[21–23]. It is a combination of a MOT and a well established methodology called RIMS (recoil ion momentum spectroscopy). MOTRIMS makes use of conservation of energy and momentum in ion-atom collisions to ultimately determines the average relative population of the different states in a MOT.

As it is obvious from the equation 1.2 that the excited fraction is expected to vary as a function of intensity and detuning, a range of intensities and detunings were used for these measurements. In order to make the study more comprehensive we also measured the effects on the excited fraction of other MOT parameters like intensity balance in the trapping beams, B-field gradient and laser repump intensities. A new method for the laser spot size measurement has been introduced to reduce the uncertainty in intensity measurements[24]. For precise control of laser frequency, new locking and detuning schemes were implemented.

The measured excited fraction data were compared with theory, and recommendations were made as to the confidence with which one can know the excited fraction.

The rest of the thesis is organized as follows: Chapter 2 describes several theoretical models and a generic preview of the MOT for better understanding of what follows. Chapter 3 is a complete description of the apparatus used in the experiments. This includes the information about the trapped atoms, laser locking and intensity measurement, a description of the diagnostic technique, MOTRIMS, is also included in the same chapter. The data processing and acquisition for this work is discussed in Chapter 3 as well. Chapter 4 contains analysis and measured results and also comparison with theory. Chapter 5 summarizes the work and suggests some future research directions. The thesis ends with an inclusion of bibliographic notes and appendices.

Chapter 2

Theoretical Models

The main focus of this work is to measure the excited fraction in a MOT, independent of any theoretical model, and then to test existing models for their validity using these data.

The theoretical machinery necessary for comparison with the experimental results, is presented in this chapter. The simple two-level model gives insight into light-atom interaction and the dependence of excited fraction on laser intensity and frequency. This simple model is widely used in the cold atom community and is discussed in Section 1. Models that are suitable for MOT configurations are discussed in Section 2. Section 2 also contains the principles for the operation of a MOT in order to better understand mechanisms by which atoms interact with the trapping laser radiation. Classical light fields and quantum mechanical atomic systems are assumed throughout the discussion.

2.1 Excited Fraction For Simple Systems

A coherent travelling optical electromagnetic wave interacting with a dilute atomic gas with a frequency approximately equal to the Bohr transition in a two level atomic system transfers population from the ground state to the excited state. The population may decay back to the ground state either by spontaneous or stimulated emission. For a low intensity optical beam, a population balance is established between the two levels and the excited population can be up to 50% of the total population.

The population oscillation between the two levels is called the Rabi frequency which is determined by the coupling strength between the two levels and is given by

$$\Omega(t) \equiv \frac{-qE_0}{\hbar} \langle e|\vec{r}.\hat{\epsilon}|g\rangle \,. \tag{2.1}$$

Here e and g are excited and ground state wave functions, and $\hat{\epsilon}$ and $q\vec{r}$ are field polarization and dipole moment, respectively. The field strength is given by E_o. Moreover, assuming electric dipole transitions and that the dipole moment and polarization of the electric field are in the same direction, the Rabi frequency becomes

$$\Omega \equiv \frac{-eE_0}{\hbar} \langle e|r|g\rangle \tag{2.2}$$

The dynamics of a system undergoing laser-atom interaction can readily be described by the optical Bloch equations[25,26] in a density matrix formalism. The time dependent population densities can be written as

$$\frac{d}{dt}\rho_{eg} = -\left(\frac{\gamma}{2} - i\delta\right)\rho_{eg} + \frac{iw\Omega}{2} \tag{2.3}$$

and

$$\frac{d}{dt}w = -\gamma w - i(\Omega\rho_{eg} - \Omega^*\rho_{eg}) + \gamma \tag{2.4}$$

Here $w = \rho_{gg} - \rho_{ee}$, with ρ_{ee} and ρ_{gg} the populations in excited and ground state, respectively, and are related by $\rho_{gg} + \rho_{ee} = 1$. The natural decay rate is expressed as $\gamma = \Gamma/2$, with Γ the full line width and δ the detuning of the optical radiation from resonance. The matrix elements ρ_{gg} and ρ_{ee} are the ensemble averaged populations of the lower and upper atomic levels, respectively.

The steady-state solution to these equations under the rotating wave approximation yields an excited fraction[18,27] of

$$\rho_{ee} = \frac{I/I_s}{1 + 2I/I_s + (\frac{2\delta}{\Gamma})^2} \equiv f. \tag{2.5}$$

Here I is total intensity of the laser beam, and I_s is the saturation intensity given by

$$I_s = \frac{2\pi hc\Gamma}{3\lambda^3}, \tag{2.6}$$

where λ is atomic wave length. A more compact form 2.5 in terms of the saturation parameter s_0 is

$$f = \frac{s_0}{1 + 2s_0}, \tag{2.7}$$

with

$$s_0 \equiv \frac{I/I_s}{1 + (2\delta/\Gamma)^2}. \tag{2.8}$$

In the case of a low saturation parameter, $s_0 \ll 1$, the population is mostly in the ground state; for $s_0 \gg 1$ the excited fraction approaches 1/2.

The equations 2.5 and 2.7 give the excited fraction in a dilute gas interacting with a polarized, low intensity optical beam in 1-dimension. In the case of ^{87}Rb for D2 line $I_s = 3.28$ mW/cm^2.

This model gives an understanding of the physics underlying field-atom interactions; however, there are limitations to this model. For instance, if instead of a single travelling wave, one had a pair of counter-propagating beams, one would have interferences, the consequences of which are not addressed in this simple model. Furthermore, sufficiently intense fields would give rise to a.c. Stark splitting; high atom density results in radiation trapping; and external B-fields result in Zeeman splitting. None of these effects are addressed in the simple model of equation 2.5.

2.2 Excited State Fraction in a MOT

Before trying to estimate for the excited fraction in a MOT environment, it is wise to know what a MOT is and how it works. This introduction will help one understand the theory and experiment.

2.2.1 Magneto Optical Trap

A MOT is a combination of magnetic and optical traps provided by the electromagnetic coils and laser beams[28–31].

The laser beams, appropriately detuned and polarized, interact with the atoms through the Doppler shift, cooling and trapping them at a point where the B-field is zero. A commonly used quadrupole trap is shown in Fig. 2.1. This trap has zero B-field at its center with a symmetric trap depth in the x-y plane and with twice the B-field gradient along the Z-axis.

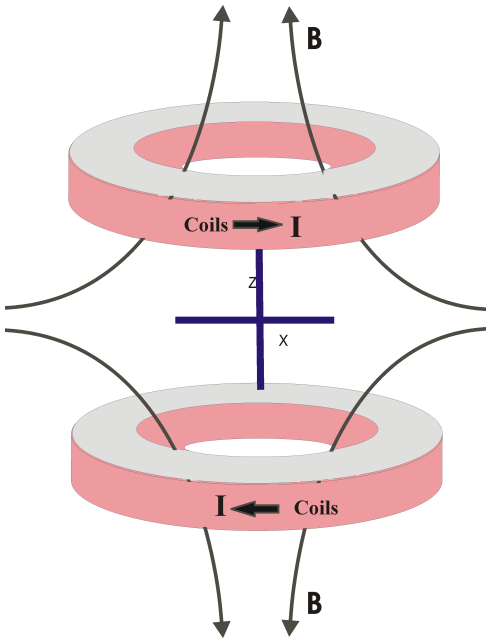

Figure 2.1: A pair of coils with opposite currents, having zero B at the center which increases approximately linearly (near the center)in every direction.

The optical pumping and strong radiation force on slowly moving atoms in a linearly inhomogeneous magnetic field controls the cooling and trapping of atoms. The B-field breaks the degeneracy in atomic transitions for the simple example scheme of $J_g = 0 \rightarrow J_e = 1$ into three Zeeman components. These three levels are excited by the polarized red-detuned light, as shown in Fig. 2.2. In this figure, depicting energy versus position along the Z-axis, a pair of circularly polarized counter- propagating beams, red-detuned by an amount δ, are incident on an atom in the vicinity of z= 0. The Zeeman effect shifts the excited states $M_e = +1$ and $M_e = -1$ up and down from the zero B-field atomic resonance.

At the position $\acute{z}$ in Fig. 2.2, the $\Delta M = -1$ transition is closer to resonance than the

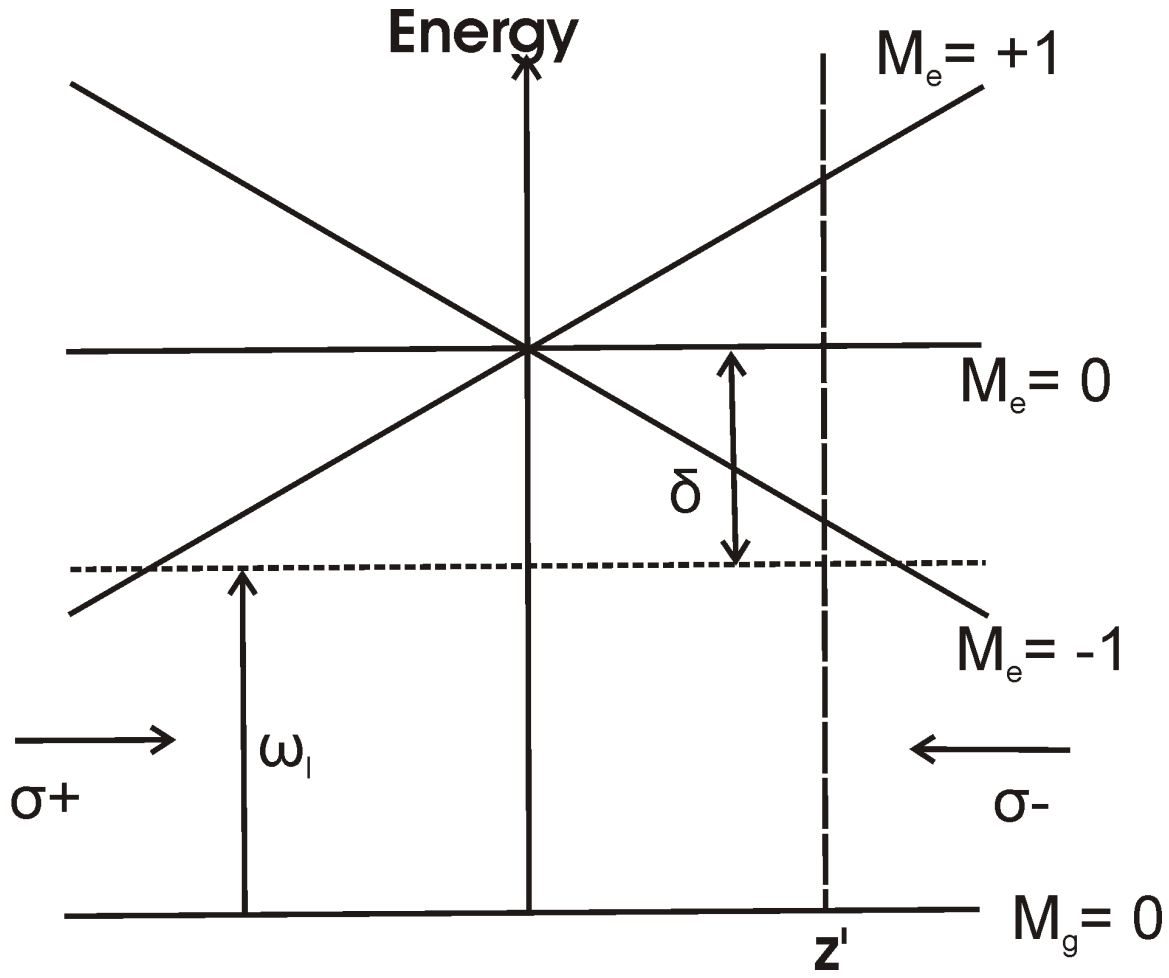

Figure 2.2: Arrangement for a MOT in 1D[27]. The horizontal dashed line represents detuning. The z' is the location where atoms is closest to the resonance with the σ_- beam.

$\Delta M = +1$. If the polarization of the laser beam incident from the right is chosen to be left circularly polarized, and from the left to be right circular, then more light is scattered from right sided beam than the left. Thus, atoms are driven toward the center where $B = 0$. A similar situation can be pictured on the left side of the figure with the right circularly polarized light driving the atoms back toward the center. The same scheme can be extended to three dimensions by using six beams instead of two, as in the actual case.

A schematic diagram of a MOT and the relevant optical helicities are shown in Fig. 2.3. As a source less B-Field gradient introduces the inhomogeneous field it is better, for prac-

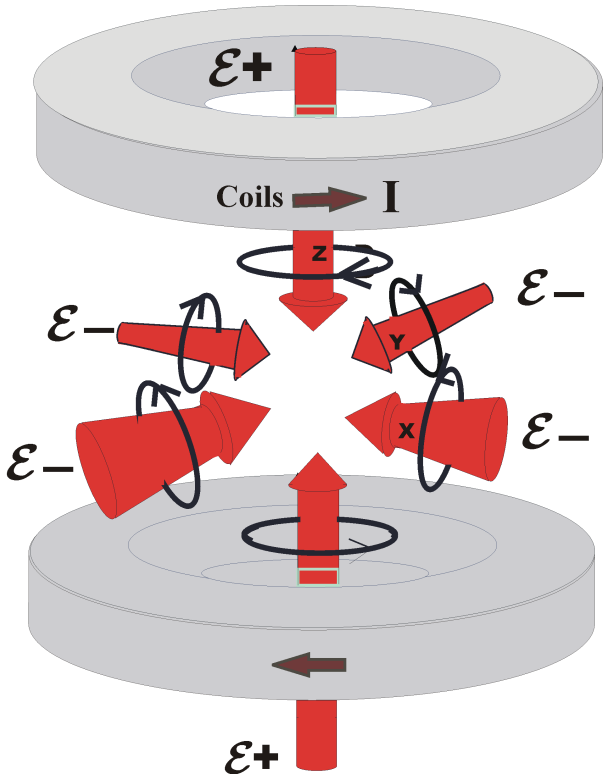

Figure 2.3: A MOT is formed from three orthogonally pairs of circularly polarized beams. All beams interact at the point where the B-field is zero.

tical purposes, to express the circularly polarized light in terms of the rotation of the net electric filed. In the figure two polarized beams are expressed as the resultant of the electric fields expressed as $\epsilon+$ and $\epsilon-$for clock wise and anti clockwise rotation[32] Three pairs of circularly polarized beams, combined with a B-field gradient, are responsible for reducing the translational kinetic energy of the atoms and confining the atoms near B= 0.

2.2.2 Modified Simple Model

As mentioned in the preceding generic preview, in a MOT pairs of polarized beams interact with atoms 3-dimensionally. This beam configuration interacts with the magnetic sublevels in the atomic system and gives position dependent transition rates. In addition to that, the polarization of the net field as well as the Rabi frequency are also functions of position. Therefore either the simple two level model should be modified accordingly or an entirely new

model should be constructed. Fortunately both approaches are available in the literature.

The two level formula was modified by the Townsend *et al.*[19] and is given as

$$f = \frac{C_1^2 I/I_s}{1 + C_2^2 I/I_s + (2\delta/\Gamma)^2}, \tag{2.9}$$

where $C_1$and C_2 are effective Clebesh- Gordon coefficients connecting ground and excited state sublevels. One might expect C_1 and C_2 to be of the same order of a magnitude, though not necessary equal. The constants C_1 and C_2 are assumed to be independent of any changes in the intensity and detuning of the laser fields.

2.2.3 Multi-level Ansatz

The construction of a new model is laborious work. However, Javanainen[20] made extensive calculations of the excited fraction as a function of intensity and detuning. He chose atomic systems having specific initial and final state angular momenta and placed them in linearly polarized linear (LPL) and circularly polarized or magnetic molasses trap (MMT) fields in three dimensions. In an LPL optical molasses one pair of laser beam shares the same linear polarization whereas the other pairs have orthogonal polarization. When the temporal phase equals zero, corresponding to phase-locked lasers, the light field is linearly polarized in space and is referred to LPL0; for random phases the light field is referred to as LPLR.

In the MMT configuration the laser beam pairs have circular polarization and 3 pairs interact with each other just as in a usual MOT described above. For the two cases when the temporal phases are either zero or random, calculations are carried out on an atom at a given position and for the appropriate temporal phases of the field. In this model, Javanainen[20] calculated the effective Clebesh-Gordon coefficients in a multilevel state. After position-averaging the Clebsh-Gordon coefficients and taking into account the spacial distribution of both light field intensity and polarization, Javanainen proposed an ansatz as follow:

$$f = \frac{y}{1 + 2y} \tag{2.10}$$

Phase	α	β	s_r
0	1.006	1.927	0.871
random	0.994	1.311	0.729

Table 2.1: Typical values of the three parameters α, β, s_r at zero and random temporal phases.

where

$$y = \left[\left(\frac{1}{\alpha} - \frac{1}{\beta}\right)\frac{s_r}{s_0 + s_r} + \frac{1}{\beta}\right] s_0. \tag{2.11}$$

Here $\alpha^{-1/2}$ and $\beta^{-1/2}$ are the effective Clebesh Gordon coefficients at low and high intensity regimes respectively. The saturation parameter s_0 is defined in equation 2.8 and s_r is the roll-over parameter which determines the switch from low to high intensity. For the low and high intensity regions, the formula behaves like a simple two level system with saturation intensities αI_s and βI_s, respectively.

Javanainen fit the results of many calculations to equation 2.10, using α, β, and s_r as the adjustable fitting parameters. His results foe $J = 1/2$ and $J' = 3/2$ are given in Table 2.1.

For future reference, we will refer to these models as the one parameter (two level equation 2.5), two parameter (modified two level equation 2.9) and three parameter (Javanainen, equation 2.10) models, respectively.

Chapter 3

Experimental Setup

This chapter is a complete description of the experimental setup used for the measurement of the excited fraction in a MOT. This setup has been divided into two main sections: system preparation and diagnostic tool box.

The system preparation section contains information about the system itself as well as the techniques and devices used to prepare it for investigations. The MOT is the main device used for the atomic systems to be studied. The salient features of this device, including its components are discussed in this section. As in this work we are concerned with the excited fraction in the MOT as a function of MOT parameters like trap laser intensities, frequencies etc, control of these variables is critical; a detailed description of their measurement and control has also been included in this section.

In the diagnostic section, the specific technique used to investigate the trapped atoms, its operation and final output will be discussed. The data acquisition system, being an integral part of the diagnostics, is also described.

Throughout these experiments an assortment of the optical elements as well as many "knobs" for the ion optics have also been used; description of all them is not a simple task. Wherever it is found necessary their descriptions are included. However, most of the time these descriptions are intentionally omitted for the sake of clarity.

3.1 System Preparation

3.1.1 Magneto optical Trap

As described in Chapter 2, a MOT generally consists of beams of circularly polarized light interacting with atoms in an inhomogeneous magnetic field. The laser field provides a mechanism for cooling and trapping atoms by supplying a velocity-dependent force, while the magnetic field creates a spatially dependent Zeeman shift in the atomic transition frequencies. These two effects together cool and trap atoms in a localized region, at a temperature well below the mK range.

The target trapped for this dissertation is ^{87}Rb, with a nuclear spin of $I = 3/2$. The fine and hyperfine structure of the ground and excited states are shown in Fig. 3.1. The ground $5s_{1/2}$ and the excited $5P_{3/2}$ states are further spit into hyperfine levels. The $5S_{1/2} - 5P_{3/2}$ transition is generally called the D_2 line. A laser with $\lambda = 780$ nm is responsible for connecting $F = 2 \rightarrow F' = 3$ hyperfine levels which is called a cycling transition since the $5P_{3/2}, F' = 3$ state can only decay into the F=2 hyperfine ground state; the natural decay time is 27 ns.

The light sources used are commercial tuneable external cavity diode lasers having outputs of 70 and 20 mW for the trapping and repump lasers respectively. Portions of the laser's outputs are used for stabilizing the wavelengths. This is done by locking to the appropriate hyperfine transitions in a separate Rb cell. The rest of the trap laser output is fed to a diode amplifier which gives an output power of approximately 350 mW. The amplifier output is then passed through an acoustic optical modulator (AOM) for detuning the trapping laser, and finally the beam is sent to the collision chamber. Before reaching the chamber the beam is split into three paths and each of which is made circularly polarized using quarter wave plates. After passing through the chamber these beams are retro-reflected, double passing through quarter-wave plates, and brought back into the chamber.

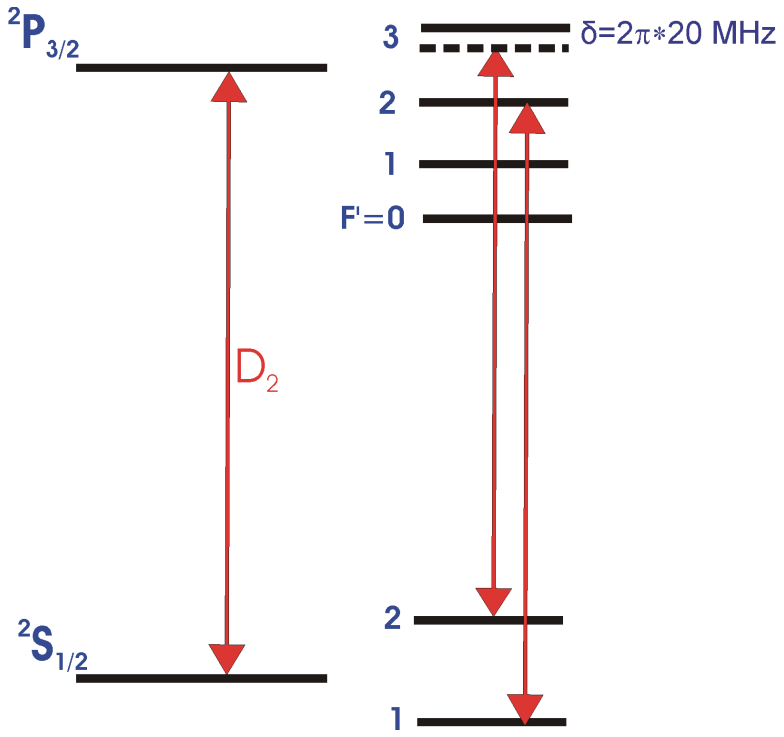

Figure 3.1: The energy level for the ^{87}Rb D_2 line. Trap laser connects $F = 2 - F' = 3$ and repump goes from $F = 1 - F' = 2$.

Hence, each of these orthogonal axes contains a pair of circularly polarized beams of light, one with an opposite helicity to the other. Each pair causes a velocity dependent cooling force to be applied to the atoms. The usual detuning of the trap laser is $-2\pi * 20$ MHz from resonance.

There is some small probability that the trapping laser may populate the $F' = 2$ excited state, as this state is in the vicinity of $F' = 3$, with an energy separation of 267.1 MHz. When this occurs, the excited population in $F' = 2$ has a 50% probability of decaying either back to the $F = 2$ ground state, where it will be back in trapping cycle, or decaying down to the $F = 1$ ground state. The ground $F = 1$ state neither interacts with the trapping laser nor decays into other levels; and as a result the atoms are free to leave the trap. This optical pumping effect is corrected by a low intensity "repump" laser at 780 nm. The repump laser couples the $5S_{1/2}, F = 1$ ground state and the $5P_{3/2}, F' = 2$ state. As the rate at which

the atoms are optically pumped into the $F = 1$ ground state is relatively low compared to the rate at which this population is excited back into the $F' = 2$ state, the repump laser efficiently keeps the population in the trapping and cooling cycle. Light from the trap and repump lasers are combined by a polarized beam splitter before going to the chamber.

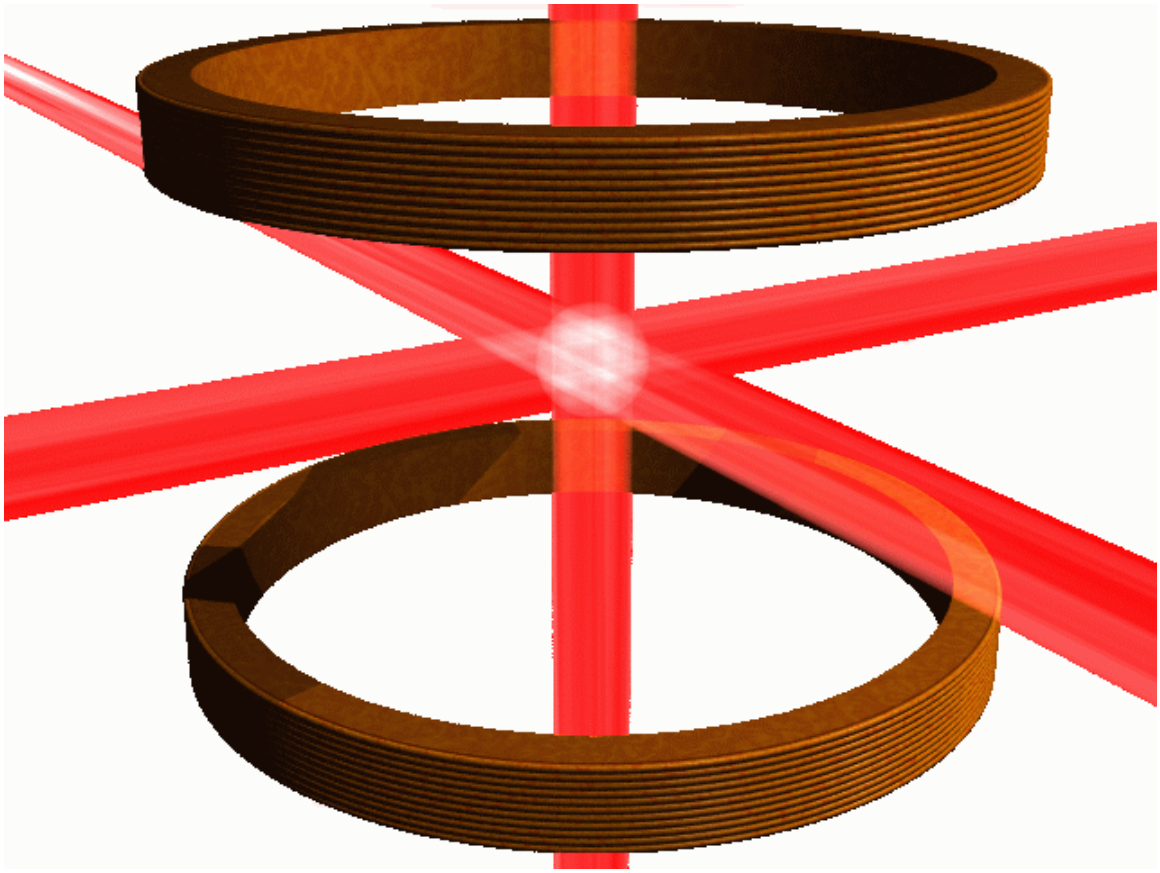

Figure 3.2: Conceptual picture of the magnetic and optical fields used for cooling and trapping. The zero B-field point is at the intersecting point of all lasers and is where the atoms get trapped[33].

In order to have a stable trap, a position-dependent force is needed for the atoms. This force is provided by the inhomogeneous magnetic field generated by a pair of coils, arranged in the anti-Helmholtz configuration. The magnitude of the B-field is zero in the center and increases as a function of position in all directions. When an atom moves away from the center of the field it experiences a B-field gradient that lifts the Zeeman degeneracy and

Parameter	Value	Units
B-Field Gradient	~ 12.45	Gauss/cm
MOT Temperature	130 ± 100	μK
Total intensity of Laser	~ 90	mW/cm^2
MOT Density	$\sim 10^8$	atoms/cm^3
Chamber Pressure	10^{-10}	Torr

Table 3.1: Typical MOT Characteristics

increases the probability that the atom can absorb a photon from the trapping laser. This absorption and emission of photons brings the atom back to the center of the trap. Together, the magnetic and optical fields cool and trap the atoms to produce a dense, cold target, shown conceptually in Fig. 3.2.

For the experiments presented here, most of the time, the magnitude of the magnetic field gradient is ~ 12.45 Gauss/cm. Table 3.1 shows the typical experimental parameters used.

Once all the experimental conditions for cooling and trapping are fulfilled, a large glowing cloud of atoms can be seen in the chamber through the use of infrared CCD cameras.

3.1.2 Laser Locking

A stable laser frequency is one of the most important requirements for many applications. There are many methods for achieving this goal, depending upon the particular laser and desired stability. Long term frequency stability and reproducibility requires locking to an absolute reference, e.g. an atomic or molecular transition.

The existing methods for frequency locking may be divided into two categories; Doppler-broadened and Doppler free. A very useful method in the first group is called dichroic atomic vapor laser lock (DAVLL)[34] and it relies on the circularly dichroic absorption in a magnetic field. Despite its simplicity, the DAVLL method offers a wide capture range and a large signal. It allows locking to a broad range in the vicinity of an atomic transition. However,

if the experimental requirement is to precisely detune the laser from an atomic resonance by a frequency of several natural line widths, the broad range of frequencies over which one can lock using the DAVLL poses limitations to the precise measurement of those detuned frequencies.

One of the techniques for long term, precise and stable frequency reference is called Doppler-free saturated absorption spectroscopy (DFSAS)[35,36]. Using DFSAS, a laser can be locked to an individual hyperfine peak rather than some arbitrary frequency in a Doppler-broadened peak.

In DFSAS, a portion of the output of the laser is split into three beams, two less intense probe and reference beams and a more intense pump beam. The pump beam is allowed to overlap with the probe beam and travels anti-parallel to it. The pump beam is partially absorbed by atoms in the cell whose velocity distribution is such that the laser frequency is resonant with an available atomic transition. Similarly, the probe beam also interacts with a group of atoms having a particular velocity distribution. Because the two beams are passing through the Rb cell in nearly opposite directions only atoms that are nearly stationary can simultaneously absorb light from both lasers.

The apparatus for the Doppler-free saturated absorption spectroscopy of Rb is shown in Fig. 3.3. The output of the laser is split into three beams, the pump, probe and reference beams, at the thick beam splitter. The reference and probe beams co-propagate whereas the pump travels anti-parallel to the probe beam inside the cell. As the probe and reference beams travel in the same direction, subtracting the absorption signal of the reference beam from that of the probe beam results in a cancellation of the underlying Doppler-broadened portion of the absorption signal leaving only the Doppler-free absorption spectrum. A typical DFSAS spectrum is shown in Fig. 3.4. The peaks labelled 1, 3, and 6 are the resonances between ground $F = 2$ to excited $F' = 1,\ 2,\ 3$ hyperfine levels and peaks labeled 2, 4 and 5 are "cross-over" peaks between the 1 and 2, 1 and 3, and 2 and 3 hyperfine levels of the

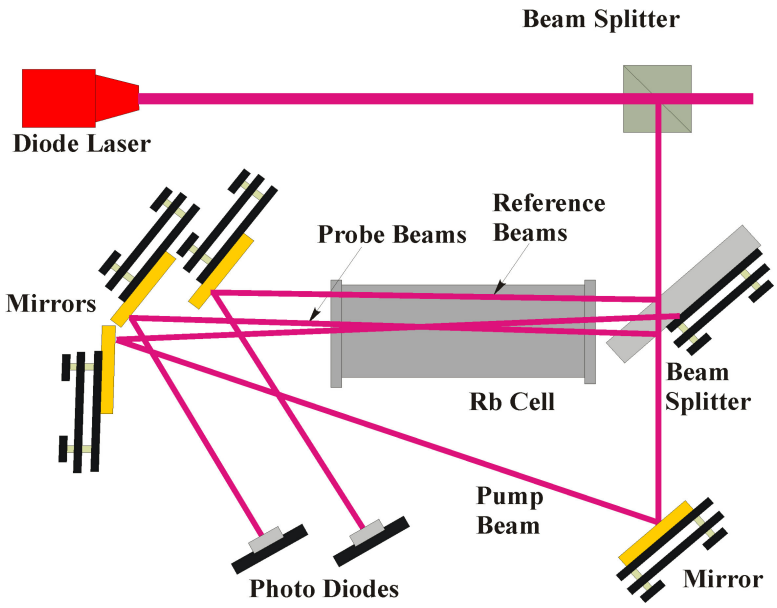

Figure 3.3: Laser beams are made to pass through the Rb cell. The pump and probe beams overlap within the cell. The reference beam travels in the same direction as the probe beam but does not overlap with the pump beam. Both probe and reference beams are detected by photodiodes

$5P_{3/2}$ level.

When the laser frequency is halfway between two transitions originating from the same lower level, cross over peaks appear because a particular velocity group of atoms will be red-shifted into resonance with the pump laser field, while this same velocity group will be blue-shifted into resonance with the probe laser field.

The 2-3 crossover peak (peak 5 in Fig. 3.4) is used as the trap laser locking peak because of its relatively dominant size and also because it is close to the cycling transition frequency. The energy spacing between the $F = 2 - F' = 3$ trapping laser and the 2-3 crossover is about 133.5 MHz.

3.1.2.1 Laser Dither Locking

In a laser dither locking scheme, a voltage signal having small dither frequency ($\sim$ 15 Hz) is applied to the laser frequency control, causing the laser's output frequency to shift propor-

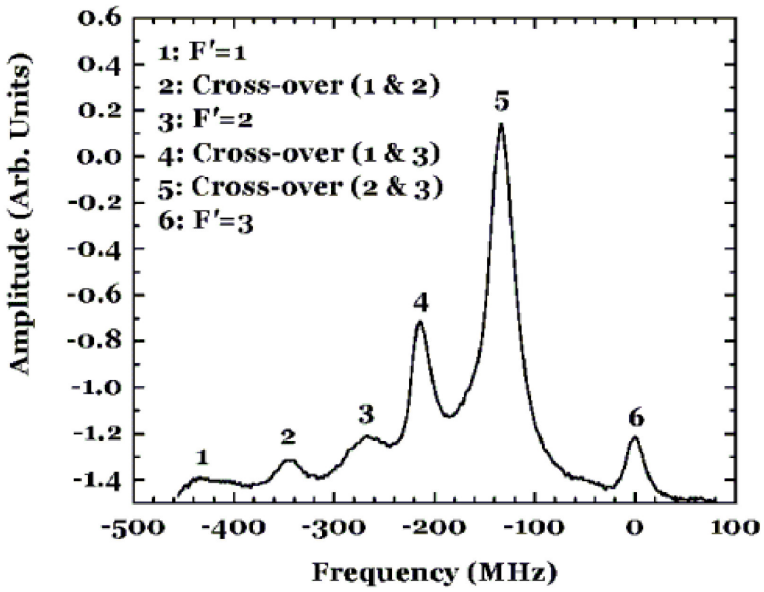

Figure 3.4: The transitions in the D2 line of ^{87}Rb are shown. The cross-over peaks are labeled as 2, 4, 5, respectively.

tionally to the amplitude of that applied signal. Therefore, the choice of dither amplitude determines the effective range of the absorption spectrum to be swept.

An electronic circuit shown in the Appendix A.1 is used with laser to lock the trap and repump lasers to desired peaks in a DFSAS spectrum. It is not necessary to describe details of the electronic components in the circuit but a graphical explanation is useful and is given below.

The simulation of the desired signal peak in the DFSAS spectrum, shown in the upper trace of Fig. 3.5a is multiplied by a square wave reference signal shown in the lower trace of Fig. 3.5a, resulting in the curve of Fig. 3.5b. If the laser frequency is centered about the desired peak, exactly half of the product will be inverted. Integration of this product results in zero and thus a zero volt signal is fed back to the laser as a correction.

If a drift in the laser frequency occurs as shown in Fig. 3.5c, the product of the DFSAS signal with the reference signal will not be exactly symmetric about zero, and thus the

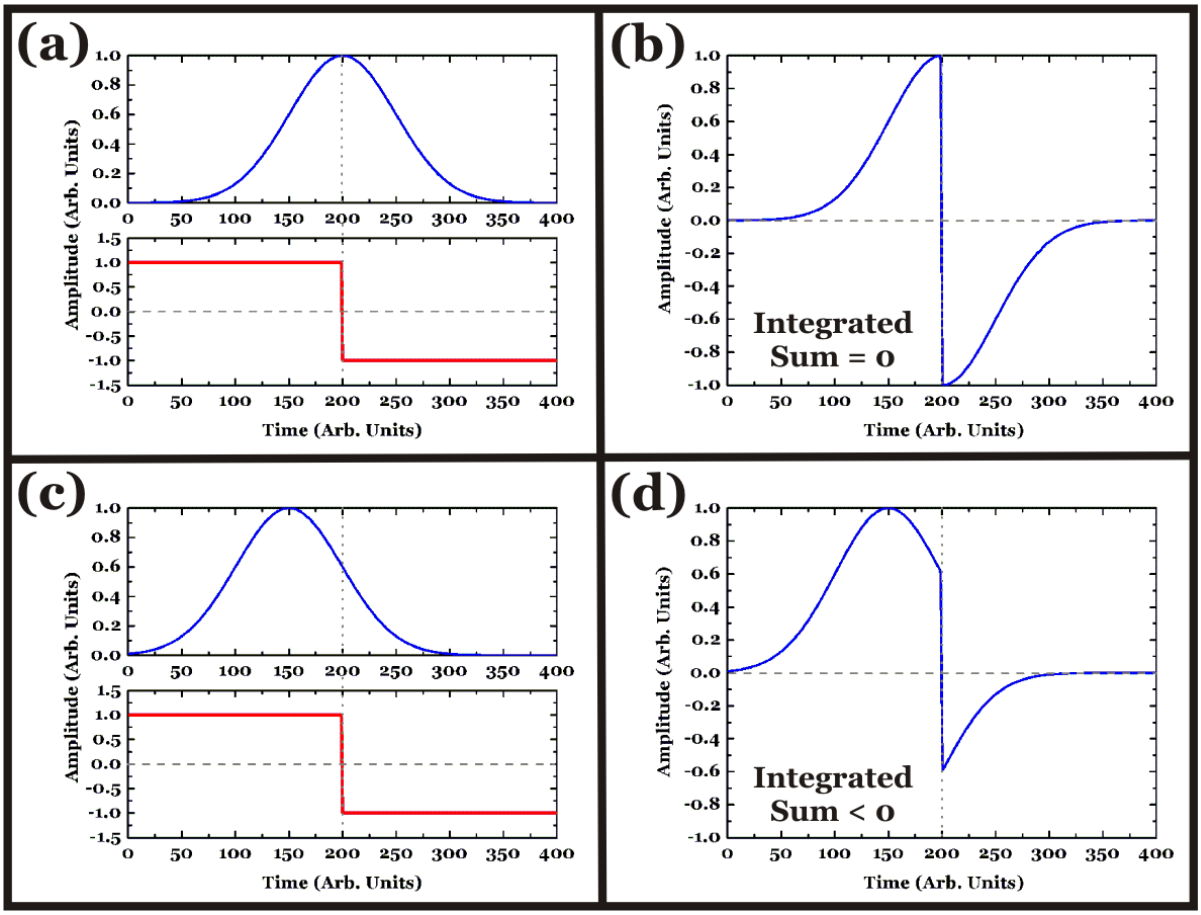

Figure 3.5: Graphical description of laser lock electronics.

integrated signal will not be zero. This non-zero output signal is fed back to the laser producing a frequency shift that returns the laser frequency to the center of the peak. In this way, the laser can be locked to an absolute reference peak.

Laser dither locking[37], though robust against many disturbances, like acoustical noise, large ambient temperature variations, or other sources of interference, has some drawbacks too. For instance, by dithering the laser, its effective line width is increased. For the experiments described in this thesis, in which trap laser detuning is believed to be a critical parameter, it is desirable to control the laser frequency as tightly as possible. Therefore, although the laser-dither is acceptable for the repump laser, an alternate technique was used for the trapping laser.

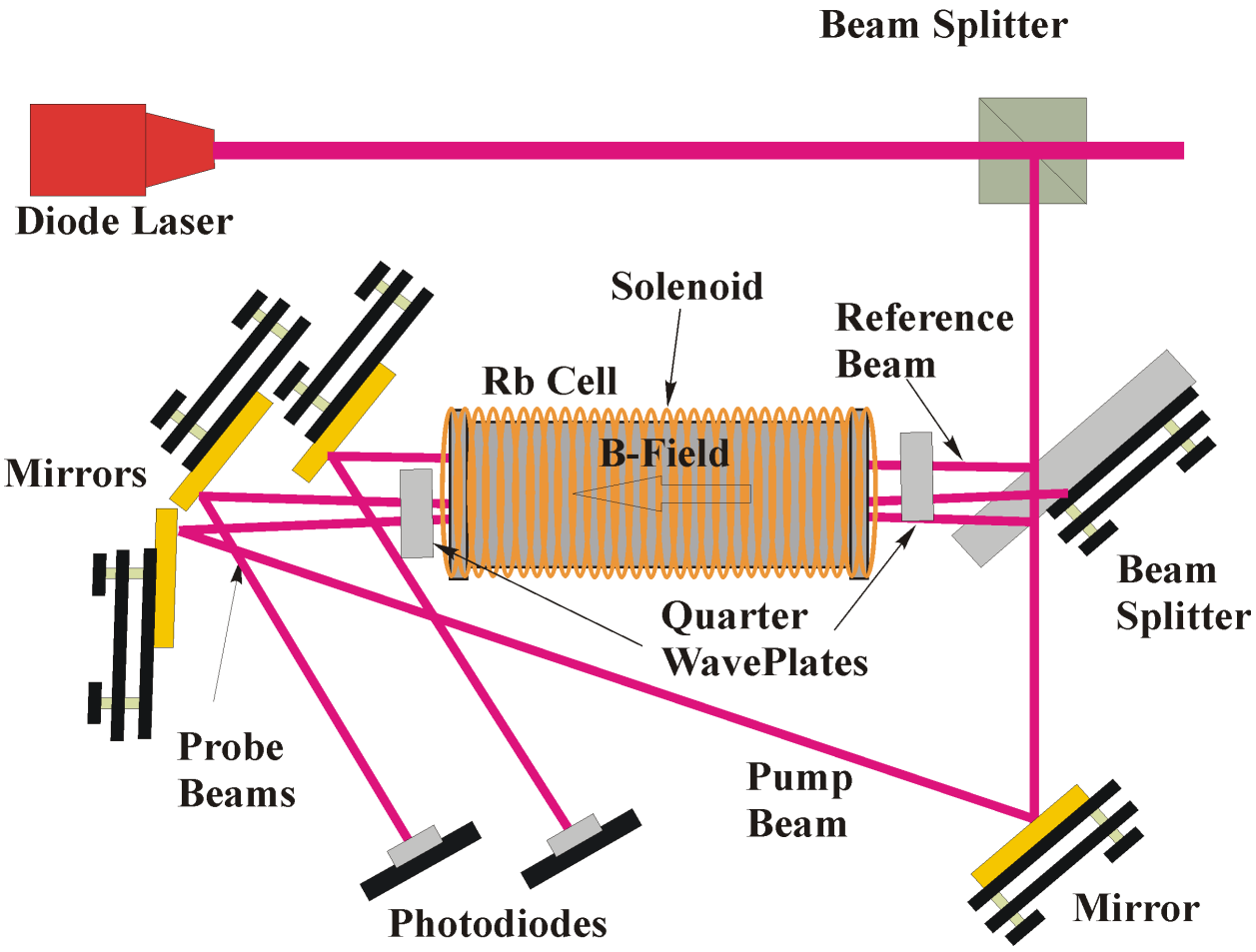

Figure 3.6: Pump and probe beams are interacting with atoms in the cell immersed in a B-field. B-field Zeeman splitting dithering is responsible for locking the laser in this scheme

3.1.2.2 B-Field Locking

The locking apparatus including a magnetic field is shown in Fig. 3.6. The optical setup is unchanged, except for the addition of a solenoid wrapped around the rubidium cell and two quarter wave plates used for pump and probe beams.

The basic electronics used are the same as well, except instead of laser frequency, the solenoid current and therefore the B-field in the cell is dithered[38,39]. This B-field dithering essentially results in Zeeman-shifting the absorption line back and forth past a fixed laser frequency, rather than dithering the laser frequency past a fixed absorption line. The same

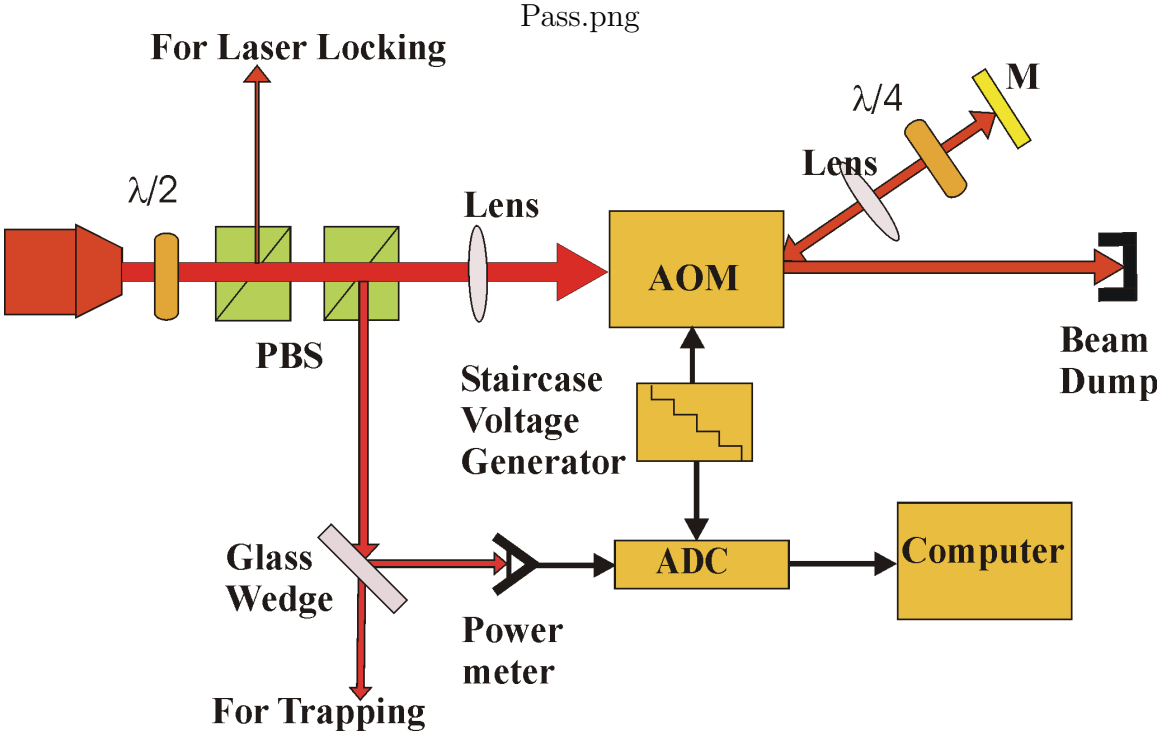

Figure 3.7: Double pass AOM configuration to avoid the steering effect.

technique of integrating over a peak is employed, and the lock electronics function identically to the laser dither locking description given above. The main advantage for using the B-field locking is that the laser field is much more stable as the laser frequency by itself is not being dithered. Only when the locking electronics detect that the absorption spectrum has changed (again, due to ambient temperature variations, acoustical noise, *etc.*) is a correction signal applied to the laser frequency. This eliminates the effective laser line width broadening inherent in the laser dither method.

3.1.3 Frequency Detuning; Double Pass AOM

In normal operation of an AOM (acousto-optical modulator), an acoustic beam and optical beam interact with each other a medium. Through the conservation of momentum between phonon and photon, the frequency of the laser light is shifted an amount equal to the acoustic frequency.

An AOM modulated laser beam makes an angle with the principle beam depending upon the frequency of the acoustic modulation. As a result, after the AOM laser beam shifted by different acoustic frequencies follow different paths going to the chamber. This unacceptable steering of the trapping laser was circumvented by double-passing the laser beam through the AOM. A quarter wave plate is used after AOM and the back-injected beam is separated from the principle one by a polarizing beam splitter. The double pass setup is shown in Fig 3.7. The primary beam is sent to a dump and the doubly modulated beam is sent to the chamber for trapping purposes.

This frequency shift can be tuned via the AOM control electronics. A schematic diagram of these electronics is shown in Appendix A.2. The controller adjusts the RF frequency applied to AOM and, hence, controls the detuning, δ, of the trapping laser from resonance.

As an example, an RF frequency of 56 MHz shifts the trap laser frequency by 112 MHz making $\delta/2\pi = -133.5 + 112 = -11.5$ MHz for a detuning of -3.4 line widths.

In order to measure the excited fraction as a function of various values of detuning, an electronic frequency shifter is applied to the AOM. A schematic of the frequency shifter can be seen in the Appendix A.3.

This circuit shifts the RF and therefore the laser frequency in sixteen equal steps. The range of frequency shifter is chosen to be from $104 - 122$ MHz. This corresponds to values of $\delta/\Gamma = -4.9 \rightarrow 1.57$. A measured one to one correspondence between each step and detuning frequency can also be seen in the Appendix B.

3.1.4 Intensity Measurements

Accurate measurement of the laser intensities, like the frequencies in the previous section is critical in the present experiments. Hence a great deal of effort has been extended to measure intensities as accurately as possible. Often a laser beam intensity has a Gaussian spatial distribution, peaking at the center and generally having different widths in x and y.

A 2D Gaussian function for an intensity at any point in space is written as

$$I(x,y) = I_0 \exp^{-2\left[\frac{(x-x_0)^2}{w_x^2}+\frac{(y-y_0)^2}{w_y^2}\right]} \tag{3.1}$$

Here I_0 is the peak intensity, w_x and w_y are e^{-2} half widths in x and y respectively, and x_0 and y_0 are the coordinates of the beam center. The peak intensity is then

$$I_0 = \frac{2P}{\pi w_x w_y}, \tag{3.2}$$

where P is the total power in the beam.

The known sources of uncertainty in intensity are laser power fluctuation, uncertainty in power measurement due to the power meter error, and the beam size measurements. The power meter used has NIST-traceable error of less than 2%. The beam spot size measurements are made by a novel method which reduces the uncertainties by a considerable amount as described below.

3.1.4.1 Measurement of Laser Spot Size

The boundaries of an optical beam are not clearly defined and consequently, the dimensions of the beam are also hard to define. A commonly used definition of the beam half width is the point at which beam intensity has fallen to $1/e^2$ of its peak value when measured in a plane orthogonal to the optical axis. This is the definition of the width we used in our beam size measurements.

A common method for measuring a laser beam spot size called the knife edge method is used to generate the beam profile. A razor blade is mechanically driven by a known distance across the beam, while the unblocked portion is measured by a power meter. Traditionally these data (*i.e.* the measured power verses knife edge position) are differentiated and fit to a Gaussian to obtain the width of the beam. In our measurement, instead of using the traditional method involving differentiation, we fit the raw data to an analytical approximation to the complementary error function. As a result, fitted parameters were obtained and

were found to be consistent with the standard Gaussian fit approach within one standard deviation, but with smaller uncertainties. A short description of the method used is given below.

Generally, for a Gaussian beam the idealized power measured for each knife position x can be written as

$$s(x) = \int_x^\infty \int_{-\infty}^\infty I(x', y')dy'dx' = I_0 w_y \sqrt{\pi/2} \int_x^\infty \exp\left[-2\frac{(x' - x_0)^2}{w_x^2}\right] dx'. \tag{3.3}$$

The integral on the right side can not be integrated analytically for arbitrary x. The common practice is to differentiate the measured $s(x)$ with respect to x which gives a Gaussian dependence on x. A Gaussian function is then fitted to the derivative of s and w_x is extracted.

But for a Gaussian noise R(x) added to the measured signal a realistic measured value would be

$$S(x) = s(x) + R(x), \tag{3.4}$$

with $R(x)$ a probability distribution defined as

$$P(R) = \frac{1}{\sigma\sqrt{2\pi}} \exp\left(-\frac{R^2}{2\sigma^2}\right). \tag{3.5}$$

Here σ is a standard deviation.

The derivative of the new measured signal with noise is

$$\frac{dS(x)}{dx} = g(x) + D(x). \tag{3.6}$$

The probability distribution for D(x) for small discrete steps in x with a spacing ϵ is found to be

$$P(D)dD = \frac{1}{\sigma'\sqrt{2\pi}} \exp\left(-\frac{D^2}{2\sigma'^2}\right)\ dD, \tag{3.7}$$

where $\sigma' \equiv \sqrt{2}\sigma/\epsilon$ and is the effective standard deviation. The effective standard deviation has dependence on step spacing ϵ. That means that the smaller the step size in the measurement, larger the scatter in the derivatives of the data. On the other hand, if larger step

sizes are taken, the fit to a Gaussian is less reliable since fewer data points are used in the fit.

In this work, instead of differentiating the data, we fit the data to the complementary error function which is related to the error function by

$$\mathrm{erf}(x) = 1 - 2\ \mathrm{erfc}\left(\sqrt{2}x\right). \tag{3.8}$$

Then the complementary error function can be expressed as

$$\mathrm{erfc}(u) = \frac{1}{\sqrt{2\pi}} \int_x^\infty \exp\left(-\frac{u^2}{2}\right) du. \tag{3.9}$$

The measured signal can then be written as

$$s(x) = \frac{P}{2}\left\{1 - \mathrm{erf}\left[\frac{\sqrt{2}\,(x - x_0)}{w_x}\right]\right\}, \tag{3.10}$$

where P is the total power when $x \to -\infty$. As already pointed out, the error function can not be integrated analytically, however several good approximations to the error function exist. These approximations can be used for a sufficiently accurate fit. The following approximation[40,41] is found to give a good fit to our data:

$$\begin{aligned} &\mathrm{erf}(x) = 1 - \left(a_1 t + a_2 t^2 + a_3 t^3\right)\exp\left(-x^2\right) + \epsilon(x), \qquad t = (1 + px)^{-1} \\ &p = 0.47047 \qquad a_1 = 0.3480242 \qquad a_2 = -0.0958798 \qquad a_3 = 0.7478556 \\ &\left|\epsilon(x) \leq 2.5 \times 10^{-5}\right|. \end{aligned} \tag{3.11}$$

A comparison of the results obtained by differentiation of the data, to that obtained through the use of the complementary error function is shown in Table 3.2

Table 3.2: Summary of laser spot size measurement using two different techniques.

Num. of points	w_{erfc}	$w_{derivative}$
50	1.97 ± 0.02	1.8 ± 0.11
100	2.01 ± 0.01	2.03 ± 0.13

An important point to be noted is that even if, in some cases, the width for both fitting techniques came out virtually same, the estimate of uncertainties in the new technique is an order of magnitude smaller than in the conventional Gaussian fit method.

3.2 Population Measurement method

In order to measure the relative populations of different states in an atomic system, one can use the ion-atom collision technique. During an ion atom collision one may wish to measure the change in the internal energy of the system. In doing so one needs to measure the final state of the system with sufficient resolution to distinguish the differential change transfer channel of interest. The kinetic energy gain or loss of the projectile and recoil determines the internal energy difference; $Q = E_i - E_f$ of the system. An important method of measuring the change in internal energy or Q-value is to measure the target ion momentum vector. This technique is commonly known as recoil ion momentum spectroscopy (RIMS). RIMS is a technique in which one measures the momentum components of the recoiling target ions after charge transfer during the course of collision with a projectile ion.

However, this measuring technique faces a serious challenge from the initial momentum spread of the target atoms. The use of a supersonic gas jet has helped to overcome this problem. Using this approach a temperature of the order of few mK in the transverse direction of the atomic beam has been achieved. RIMS applied to a cold target is called cold target ion momentum spectroscopy COLTRIMS[42–45].

A magneto optical trap can also be used in RIMS measurements since the temperature of laser-cooled atoms lies in the few hundred of μK regime. This method is then called MOTRIMS. This technique has certain merits over the traditional COLTRIMS technique. The initial momentum spread is lower since the target temperature is lower than in gas jets. The small momentum spread is uniform in all directions whereas a gas jet transverse momentum spread is lower than the longitudinal one. Moreover, it is easy to prepare

the target for study of excited target states. Laser excitation is required in laser cooling, naturally creating a cold target in some mixture of the ground and first excited state. With the introduction of additional external excitation laser fields, the population can be prepared in almost any configuration of initial excited states, or can be aligned with respect to some axis in the laboratory frame[46,47].

3.2.1 RIMS

The RIMS technique, as is obvious from the name, requires recoil ions and the instruments to measure their momenta. The recoil ions can be produced either by photo-ionization or by projectile ion collisions. The recoil ion momentum measurement requires a special spectrometer and position sensitive detectors (PSD).

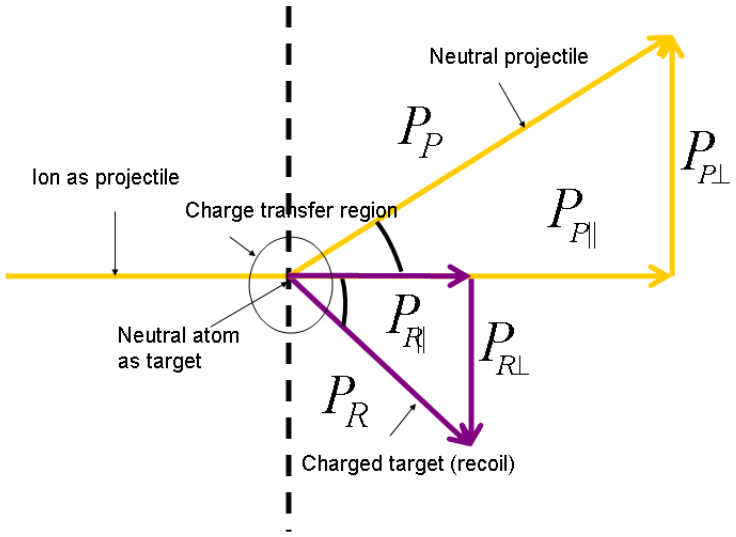

Figure 3.8: The kinematics of a single charge transfer collision, in which parallel and perpendicular momentum components are indicated.

The kinematic equations for RIMS is obtained by making use of conservation of energy and momentum. In the case of ion and atom collisions the relation between the momentum of the incident ion and that of the recoil ion is illustrated in the Fig. 3.8. Using momentum

and energy conservation the Q-value or energy defect can be expressed by

$$Q = -\frac{1}{2} m_e v_P^2 - v_p P_{R\|}. \tag{3.12}$$

Here $Q = E_{initial} - E_{final}$ is the change in internal energy of the system, v_p is the magnitude of the projectile initial velocity, m_e is the mass of an electron and $P_{R\|}$ is the longitudinal component of the momentum of the recoil ion as shown in the Fig. 3.8.

The Q-value expression of equation 3.12 assumes that only one electron is transferred in the collision process when low energy ions are allowed to collide with the target. On the right side of the equation the component of the momentum of the recoil ion lying parallel to the initial projectile velocity direction is assumed to be measured. In our experiment we set the spectrometer in such a way that this so-called longitudinal momentum is given by the recoil ion's flight time to the detector. In RIMS terminology this configuration is referred to as longitudinal extraction. One can measure the transverse component of the momentum by measuring the position of the recoil on a position sensitive detector.

3.2.2 MOTRIMS

A complete schematic of the MOTRIMS apparatus is shown in Fig. 3.9. The ion-atom collision region is inside the spectrometer; detection of recoil ions and projectiles is made on separate detectors as shown in Fig. 3.9.

The total length of the apparatus is about 3.5 m from the ion gun to the projectile detector. The MOT is made within the spectrometer which itself lies within a stainless steel chamber. A beam of Na^+ at 7 keV energy passes through some ion optics and a small aperture of 0.5 mm diameter in the first spectrometer plate. This first plate is solid plate except for the aperture and is called the pusher plate Fig. 3.10. The pusher plate is attached to a power supply and "pushes" any positive ions formed inside the spectrometer as a result of an ion-atom collision. If charge transfer occurs the Na becomes neutral, rendering Rb^+,

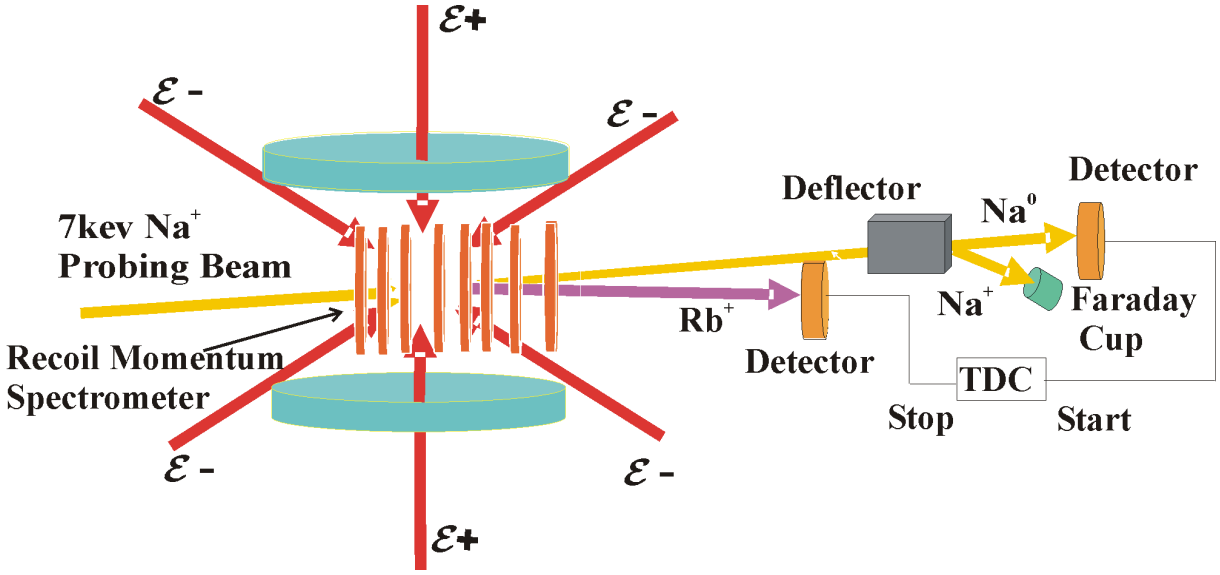

Figure 3.9: The MOTRIMS experimental apparatus. An ion beam is probing the MOT and neutral projectiles and charged target's time of flight is measured by a TDC.

and both the neutral projectile and charged recoil are detected on the downstream detectors. All projectile ion, not taking part in a collision are dumped into a Faraday cup by way of an electrostatic deflector before the projectile detector.

The momentum spectrometer has three regions, two with fields and one field-free. The Rb^+ ions are pushed and focused by the fields in these regions and are detected on the position sensitive recoil ion detector. The projectile and recoil beams are spatially separated at the recoil ion detection region because the recoil detector's axis is set 3° from the projectile axis. The effect of this angular difference on the Q-value is then corrected in software. The typical size of the MOT cloud is around 0.5 mm and the typical ion current is about 150 pA. The collision region, having finite size, might conceivably effect the flight time resolution of the spectrometer. This problem is fixed by using the appropriate electric field geometry and optimum placement of the recoil PSD. Once the Na^0 hits the detector the resulting signal starts a timer (labelled TDC for time-to-digital converter in Fig. 3.9) and the detection of Rb^+ stops the timer. The time lapse between the two events is called the time-of-flight

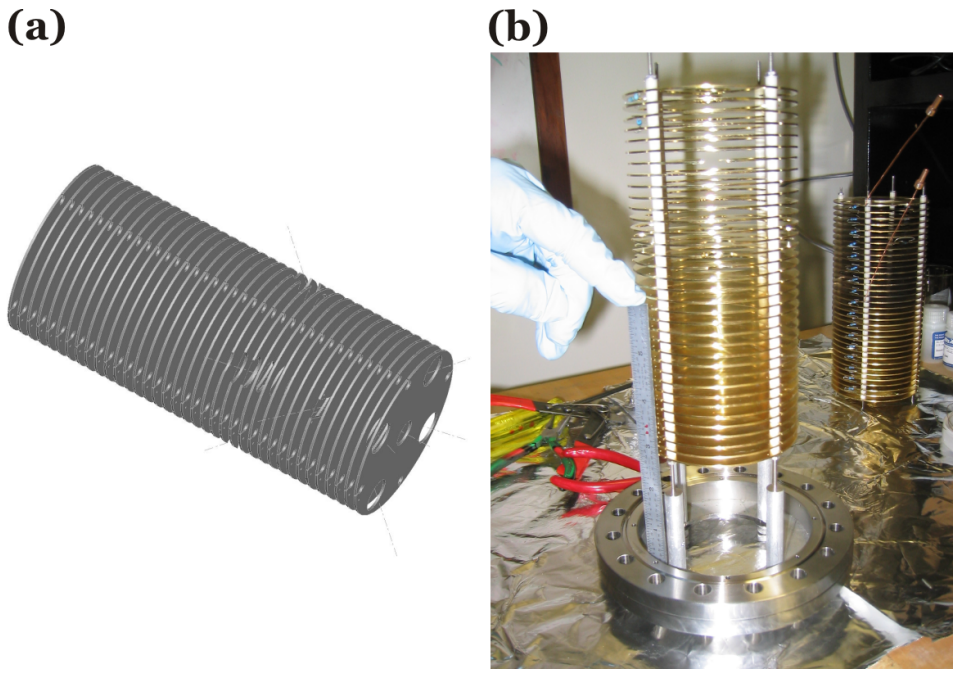

Figure 3.10: Different views of the momentum spectrometer. In (a), a solid pusher plate with holes in the center and on the edges can be seen. The central hole is for ions to pass through whereas the edge holes are for laser beam access. In (b) the spectrometer is ready to put into the chamber[33].

(TOF) which gives $P_{R\|}$ and eventually a Q-value. The time of flight measurement is made in event-by-event mode. The important parts of the MOTRIMS apparatus are described in greater detail below.

3.2.2.1 Momentum Specetrometer

The spectrometer consists of the solid pusher plate and 34 rings, shown in Fig. 3.10. The plate and rings are connected together in series with 1 MΩ resistors. The solid plate has a voltage applied to it (typically $\sim$ 100 V), while an independent "focus" voltage $v_f \simeq 70$ V is applied to the 16^{th} ring from the pusher plate. The final electrode, number 34, is grounded and the PSD is located 1024 cm downstream from the pusher plate. The resulting field gradients focus the recoil ions in momentum space, ensuring that ions with the same recoil momentum will strike the downstream detector with the same flight time and position,

independent of the starting point.[48].

3.2.2.2 Detectors

The detectors used are based on micro-channel plate technology[49]. A resistive anode two dimensional position sensitive detector is used here to detect the recoil ions whereas a backgammon anode two dimensional position sensitive detector is used to detect neutralized projectiles. In both cases 40 mm diameter channel plates were used in the high gain z-stack configuration. A grounded copper mesh was placed in front of the plates to ensure that the drift region remains free of the electric field generated by the detector bias voltage. The voltages used in the recoil and projectile detectors are -2500 and -2800 volts, respectively. A further complete description of the detectors can be seen in H. Ngyuen thesis [49].

3.2.2.3 Projectile Source

A factory-made ion source with a complete ion optics assembly is used. It is easy to operate and easy to maintain.[49]

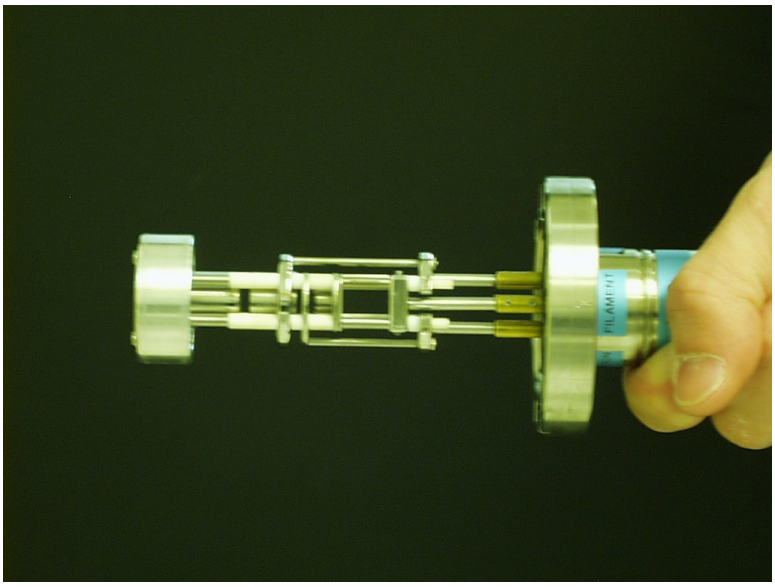

Figure 3.11: A handy ion gun assembly; the total size of the gun is about 13 cm. This part of the gun contains extraction, acceleration and focus sections along with an ion pellet stuck in the center.

The chemical compound aluminosilicate is doped with an alkali salt (here Na) and serves as a singly charged ion emitter. Simply heating the compound causes the alkali ions to "boil out". The inclusion of ion optics elements like focus, extractor, and deflector electrodes and an electrostatic lens makes this unit really handy. A picture of the ion gun unit is shown in Fig. 3.11. The ion unit provides a collimated ion beam of few a hundred nano-amps but a typical "on target" value of the current is 150 pA. The kinetic energy spread of the emitted ion is < 1 eV out of 7 keV.

3.2.3 Data Acquisition System

The main function of the data acquisition system is to move data from detectors and analog electronics to a computer via digitization, and to save the data to disk and display the most important results online.

For data acquisition, nuclear instrumentation modules (NIM) and computer automated measurement and control (CAMAC) crates are used to interface the experimental setup (detectors, laser, frequency shifter, etc) with the computer. Using the NIM units such as constant fraction discriminators, gate-and-delay generators, linear and logic fan in/out, coincidence units, amplifiers, signals are stretched and shaped and fed into the CAMAC modules (ADCs, TDC), which are interfaced with the computer via a branch highway driver (BHD).

Acquisition software enabled the secure saving of data, a real-time online display, and a data output format compatible with further off-line analysis in a Windows as well as Linux environment.

3.2.3.1 Hardware Configuration

A schematic illustration of the processing of the signals generated when a projectile hits its detector is in Fig. 3.12.

Both recoil and projectile detectors are PSDs and detect the position and time of flight

information for both collision partners. The position information signals on both detectors are detected, amplified and sent to their respective ADCs. Both time-of-flight signals are detected and amplified by preamplifiers. These amplified signals are sent to discriminators. The function of a discriminator is to read the signal and discard the noise from the strong real signal. This discrimination is done by setting a threshold level to the discriminator.

In the case of the projectile detector, the discriminated time-of-flight signal is fed to a quad fan in/out module. This module generates four outputs which are utilized in the following ways. One output is sent to a Delay/Gate module where a gate of 7.6 microsecond with a delay of 96.8 microseconds is created and fed to a coincidence module. Another output is sent to strobe the projectile ADC. The third one goes to the recoil ADC "clear" channel and the fourth is delayed for 63.5 nanoseconds and is hooked to the TDC "common" which triggers the timer.

The coincidence module is set in "AND" mode. This means that whenever it sees a signal from the recoil within the set delayed gate of projectile, it generates an output signal. Once the recoil signal is detected within the set window, an output from the coincident module is observed which is sent to another quad fan in/out whose output generates "end of window" (EOW), recoil ADC strobe, and a most important signal that stops the TDC timer. The EOW controls the operation of TDC. Thus the TDC measures the time between the projectile and recoil hits. The TOF range on the TDC is $\pm$8.3ms with a resolution of 1 nanosecond.

At the time of an event the status of the AOM frequency, laser power, and ion current is also recorded. The AOM status, power meter, and ion beam signals are sent to separate channels of the ADCs. When an event happens all ADC terminals are polled by the acquisition software. The electronics are then cleared and the system is set for the next event.

A schematic of the electronics is shown in Fig. 3.12. Blue and pink colored electronics

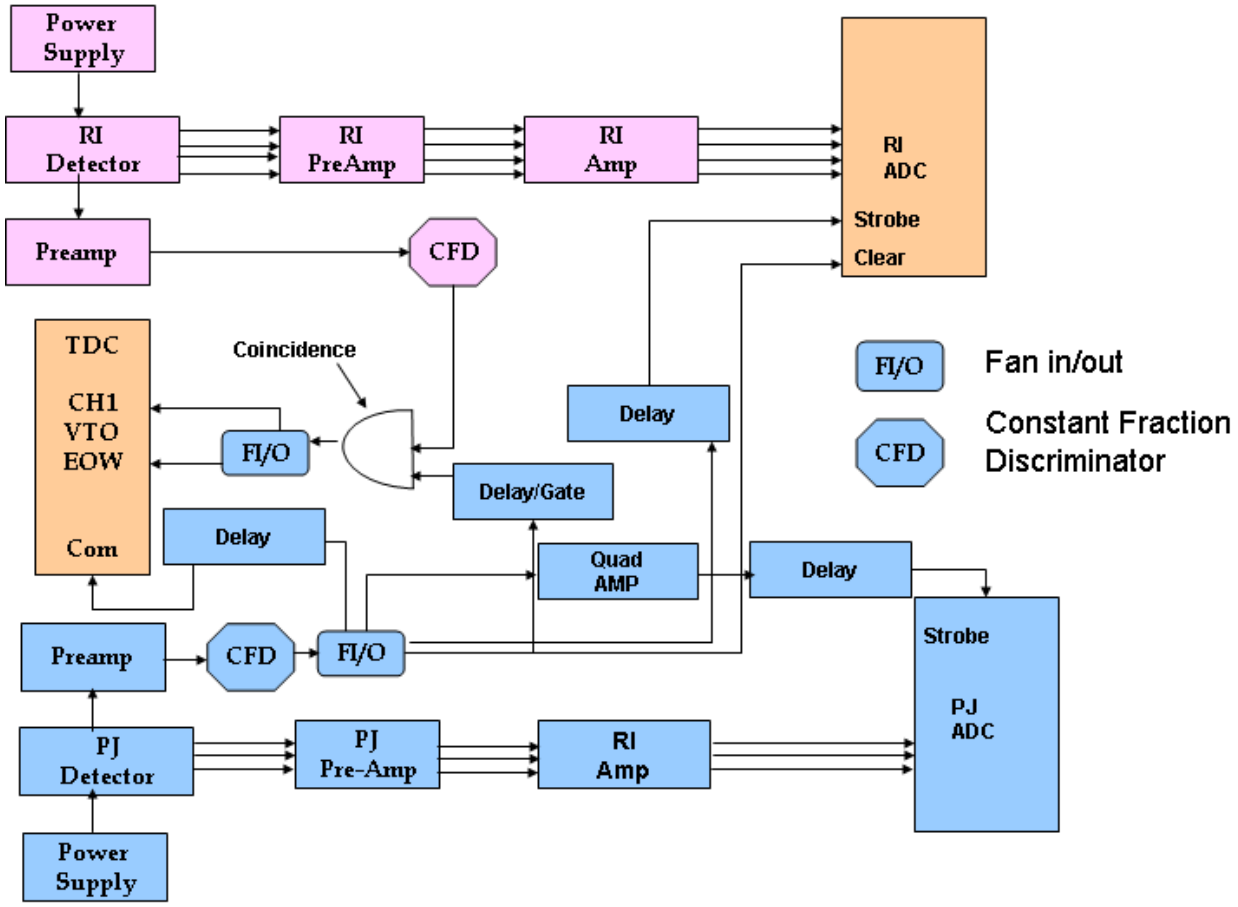

Figure 3.12: A schematic of the electronics setup used for coincidence detection. All parts are labelled according to their functions.

are the ones activated by projectile and recoil events, respectively. The electronics shown in cream color is indicative of those that receive signals from both projectile and recoil events.

3.2.3.2 Software Data Acquisition System

A "free-ware" data acquisition software package called 'SpecTCL' is used on a LINUX operating system machine. This software controls the reading, writing, and display of data from the hardware electronics discussed in the previous section. It has the ability to perform online statistics on the data too.

This program is written in C^{++} which, along with supporting header files, directs

SpecTCL on how to record or display incoming data. After an event happens, the hardware sends the data to the hard disk where it can be re-run as if it is coming from the experiment. When a session is in resort mode, the data are regenerated and thus data can be taken and re-analyzed several time using various software settings.

The recoil detector, being midway between the projectile source and projectile detector is sometimes flooded with the projectile signal. The first order effect of this is eliminated by hardware time gates but the second order effect can also be taken care by setting software gates around the particular spot on the detector where ion recoils strike. This also allows one to select regions of interest for analysis. Data can also be displayed in any convenient form. Moreover, the data can be transferred in any usable form to other users. Gates can also be set in any display window for any purpose. More importantly, cuts can be made on each Q-value channel or on any time range.

A typical operation allows one to take data indefinitely provided ion beam and target are stable. However a drift in the Q-value spectra has always been observed due to burning of the different parts of the ion gun as ion distribution within the pellet is not uniform. This drift is corrected by applying a drift lock in software.

In conclusion, manipulation of data in this a manner makes SpecTCL a powerful data acquisition package.

Chapter 4

Experimental Results

In this chapter the experimental data are presented as the first direct and complete measurement of excited state fraction in a Rb MOT using momentum spectroscopy. Direct measurements are made as a function of intensity, B-field gradient, repump power and intensity balance in the trapping beams of the MOT.

The data-taking techniques have been discussed in Chapter 3. Here the data analysis methods and results of various measurements are presented. Theoretical models discussed in Chapter 2 are tested and the general discussion about the results is included at the end of the chapter.

4.1 Data Analysis Methods

The usual set of information extracted from the hardware is the time of flight (TOF) of the recoil ion. The TOF information gives the momentum kick experienced by the recoil which gives the Q-value through equation 3.12.

The time evolution of the Q-value is obtained by sending the signal from the AOM frequency shifter to a channel of an ADC. This gives information about the laser status at any instant of time. A generic plot for the Q-value vs laser "on" time is plotted in Fig. 4.1.

Here each stripe represents the Q-value corresponding to a particular collision channel (CC) for 7 keV Na^+ projectiles and Rb ($5l$) atoms. The dominant charge transfer channels

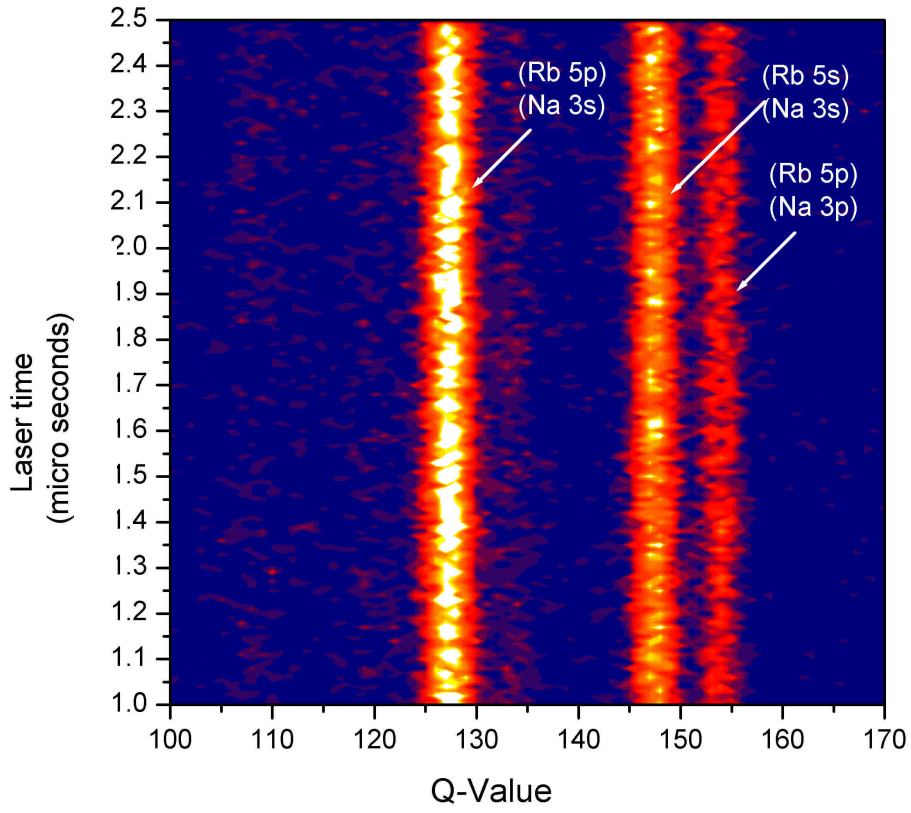

Figure 4.1: Counts are plotted versus Q-value (horizontal axis) as a function of time. The Q-value is expressed in arbitrary units.

are (5s-3s), (5p-3p), (5p-3s) and are labelled according to the electron's initial and final states on the target and projectile, respectively. The horizontal axis is the measured energy difference between the initial and final state (Q-value) and the vertical axis represents the"on" time of the trapping laser. (Note, in these experiments the trapping laser is always on. However, its detuning changes with time and can be shown on the vertical axis.) False colors of the plot represent the number of counts in each collision channel.

A downward projection of this spectrum is shown in Fig. 4.2. The channels are labelled by their final states, with the label color indicating the initial state. The colored peaks are

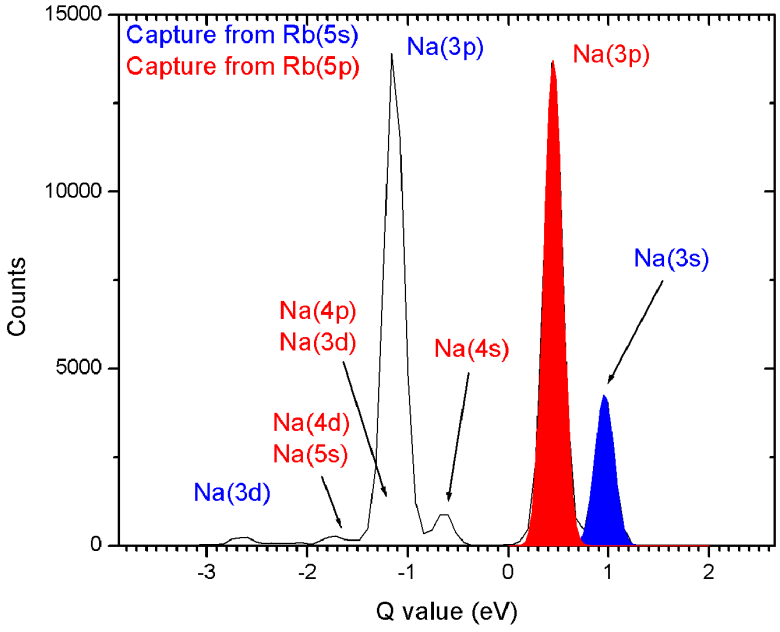

Figure 4.2: A plot of counts vs Q-Value. Here all channels are labelled according to their final states. The colored peaks used for the excited fraction measurements.

the ones used in these measurements to identify the excited fraction. Here, the areas under the peak represent the number of counts. The area under each peak therefore contains the information about the number of target atoms multiplied by the charge transfer cross section for that channel. Mathematically,

$$A_i \propto n_i \sigma_i \tag{4.1}$$

where A_i is the area of a peak and n_i, σ_i are the number of atoms in the initial state and the collision cross section, respectively. The proportionality constant contains experimental conditions like geometric factors, target thickness, and acquisition time. Measuring the peak area and cross section for each peak gives the relative number of target atoms in a particular state provided the proportionality conditions remain constant.

4.1.1 Excited State Fraction

The excited state fraction is the ratio of the number of atoms in the excited state to the total number of atoms in the MOT, and can be written as

$$f_m = \frac{n_p}{n_p + n_s}, \tag{4.2}$$

where f_m is measured the excited state fraction, and n_s and n_p are the numbers of atoms in the ground and excited states of Rb. Assuming all the experimental conditions were same throughout the measurement, the excited state fraction in terms of peak areas and relative cross sections is given as

$$f_m = \frac{A_p/\sigma_p}{A_p/\sigma_p + A_s/\sigma_s} \tag{4.3}$$

and therfore

$$f_m = \frac{A_p}{A_p + A_s R} \tag{4.4}$$

where A_p and A_s are the areas of the red and blue peaks in Fig. 4.2. The relative cross section R $= \sigma_p/\sigma_s$ has previously been measured[50]to have the value $11.79 \pm .066$ for these channels and for this collision system. This gives a direct way of measuring the excited state fraction in a MOT.

For a range of detuning, a spectrum similar to that of Fig 4.1 is plotted of laser frequency versus Q-value in Fig. 4.3. A change in the frequency of the AOM results in different areas in the participating capture channels, reflecting different excited fractions. Here the y-axis corresponds to the trapping laser detuning, and the x-axis is the Q-value (in arbitrary units).

4.1.2 Analysis of The Area Under the Peaks

In this work, the area under the peaks is measured with two methods.

(1) A Gaussian distribution function

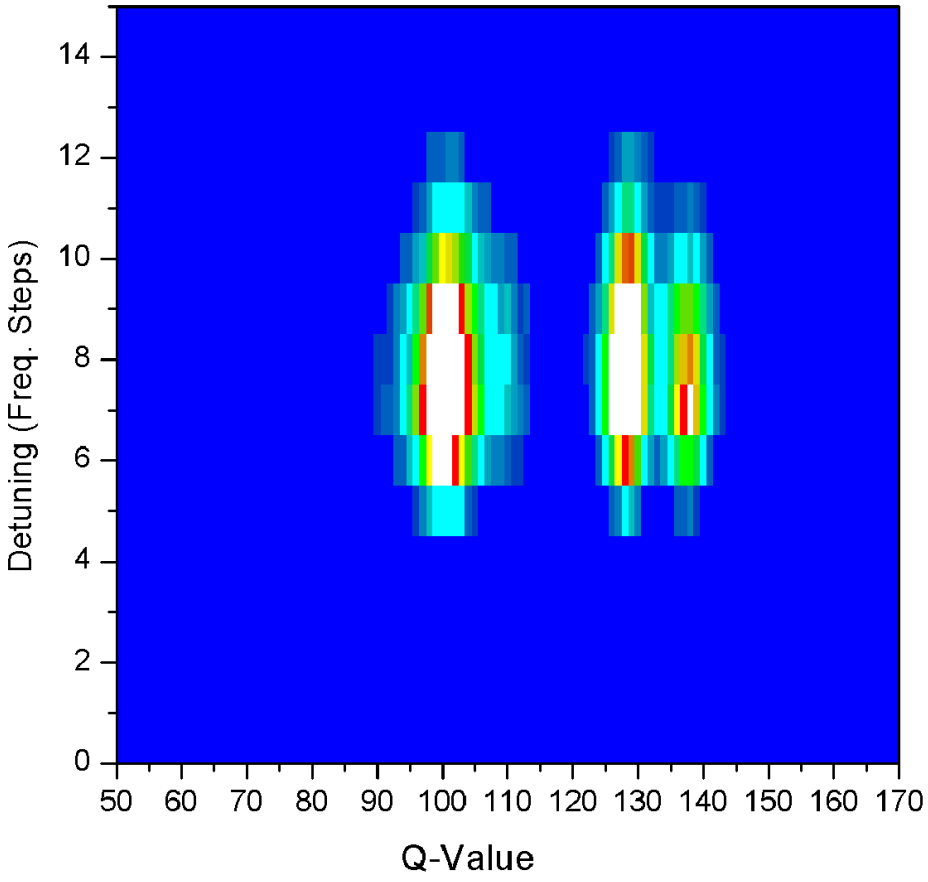

Figure 4.3: A plot of counts vs Q-value and detuning of trap laser. For each RF step the number of events is recorded.

(2) Integration under the curve.

In the Gaussian fit method, the area under a peak is fit to the Gaussian function

$$y = y_0 + Ae^{\frac{(x-x_c)^2}{2w^2}}, \tag{4.5}$$

where A is the area under the peak, w is the full width at half maximum, y_0 is the background offset and x_c is the location of the center of the peak. In the integration method, the area is measured by integrating the area under each curve. Both analysis methods were done using "Origin 7.5". Even though the background was very small, background subtraction was

made both cases. The advantage of integration is simplicity and the fact that not all peaks could always be fit to Gaussian. The advantage of a gaussian fit is that the peaks were not always complectly separated from each other, and Gaussian fits served to deconvolute the individual peak areas

For both methods simple Origin macros were written using known channel information inputs from ADCs. The results with both methods were compared and wherever the difference between the two results exceeds 2%, the data were analyzed manually. The scripts for both macros can be seen in the Appendix C.

4.1.3 Excited State Fraction Error Bars

The uncertainties in the measured value of f_m are calculated by the propagation of error technique in which uncertainties in both areas, A_p and A_s and in R were included.

The error bars on the measured excited fraction of equation 4.4 were calculated by using the following equation

$$\frac{\Delta f_m}{f_m} = \left\{ \left(\frac{\partial f_m}{\partial A_s} \Delta A_s \right)^2 + \left(\frac{\partial f_m}{\partial A_p} \Delta A_p \right)^2 + \left(\frac{\partial f_m}{\partial R} \Delta R \right)^2 \right\}^{1/2}. \tag{4.6}$$

Here ΔA_p, and ΔA_s are the statistical errors in the measured areas and ΔR is the measured error in relative cross sections. Through a simple derivation this equation can be written in terms of measured excited fraction as

$$\frac{\Delta f_m}{f_m} = f_m(1 - f_m) \left\{ \left(\frac{\Delta A_s}{A_s} \right)^2 + \left(\frac{1}{f_m} \right)^2 \left(\frac{\Delta A_p}{A_p} \right)^2 + \left(\frac{\Delta R}{R} \right)^2 \right\}^{1/2}. \tag{4.7}$$

where

$$\frac{\partial f_m}{\partial A_s} = \frac{-A_P R}{(A_s R + A_p)^2}, \tag{4.8}$$

$$\frac{\partial f_m}{\partial A_p} = \frac{f_m}{A_p}(1 - f_m), \tag{4.9}$$

and

$$\frac{\partial f_m}{\partial R} = \frac{-A_P A_s}{(A_s R + A_p)^2}, \tag{4.10}$$

have been used in equation 4.7. Here the main source of uncertainties are the areas under each peak as the uncertainty in R is small and constant.

4.2 Intensity Analysis

4.2.1 Power Calibration

In order to see the effect of laser intensity on excited state fraction, obtaining a precise value of intensity for each detuning is critical. A portion of the trapping laser beam goes to a power meter, the voltage output of which is sent to an ADC. The optical power going into the chamber is calibrated as shown in the Fig. 4.4. The total power is found to be a linear function of the power meter voltage.

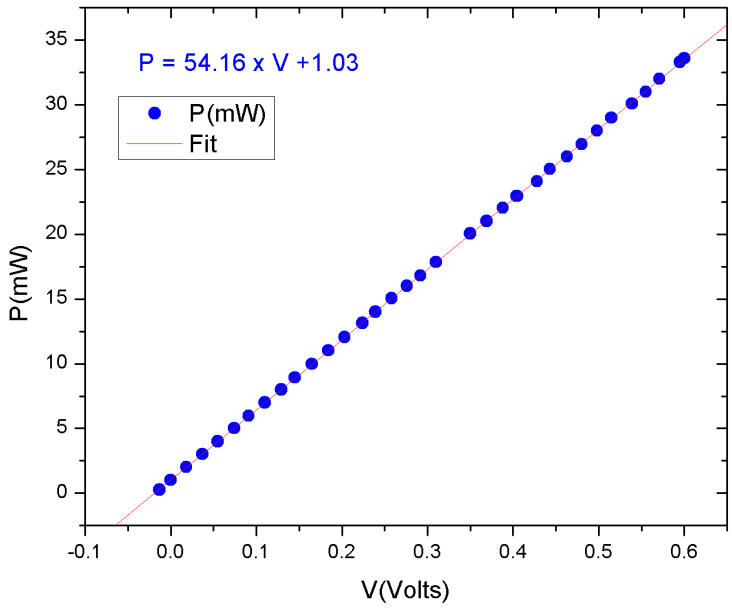

Figure 4.4: Measured total power of trapping lasers versus output of the power meter in terms of voltage signal. Laser power measured is a linear function of the output voltage.

The total power losses due to reflection at the chamber window, mirror, etc, were also measured and were included in the total intensity measure-

ment by the formula

$$I_{tot} = \frac{2\zeta(\zeta^2+1)P_{tot}}{3\pi}\left(\frac{2}{R_{HH}R_{HV}} + \frac{1}{R_{VH}R_{VV}}\right), \tag{4.11}$$

where ζ are the power losses of the beams due to reflection at each window. The R_{ij} are the radii of the beams. Here i represents the horizontal and vertical trapping beams and j represents their horizontal and vertical profiles, respectively.

The power output of the AOM is a function of input AOM frequency, and therefore the total power and hence intensity of the trap laser depends on AOM frequency. Fig. 4.5 is a density plot showing excited fraction versus laser detuning and intensity.

4.2.2 The Saturation Parameter s_0

Figure. 4.5 can show the overall trends in excited fraction, but is not appropriate for fitting the data to multi-parameter models. Rather, it is convenient to plot the measured data in terms of single parameter. In this case, the most appropriate parameter is the saturation parameter defined in Chapter 2 as

$$s_0 \equiv \frac{I/I_s}{1+(2\delta/\Gamma)^2}, \tag{4.12}$$

which takes both the detuning and intensity into account.

The value for saturation intensity used in this work is 3.28 mW/cm^2 for the ^{87}Rb D_2 line. The detuning is expressed in terms of the line width of the transition, which is about $2\pi \times 5.9$ MHz.

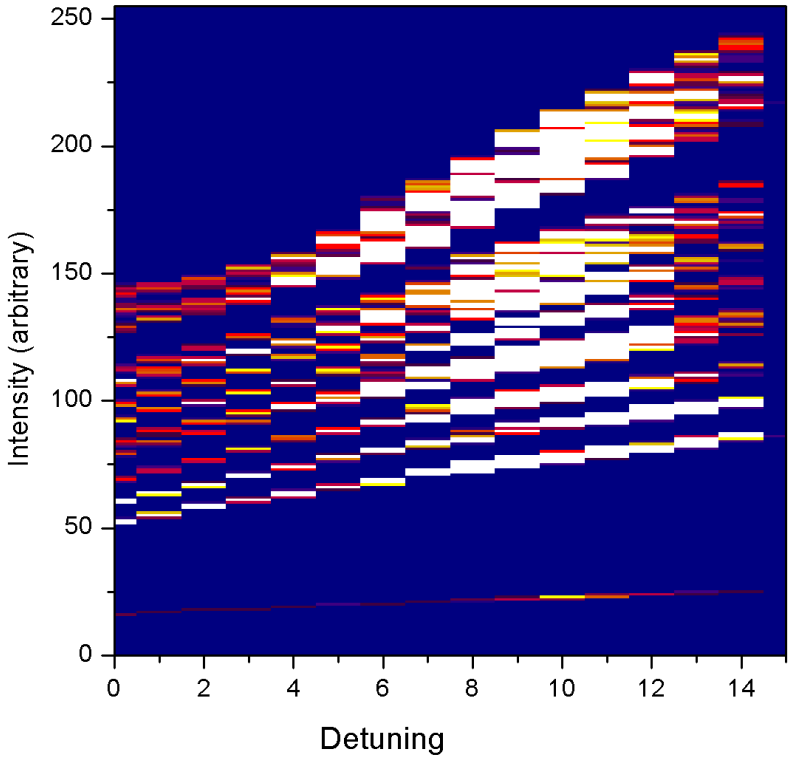

Figure 4.5: A density plot of excited fraction (in false color) as a function of trap laser intensity and detuning (in arbitrary units). For each frequency the power, and hence the corresponding intensity, is recorded.

4.3 Results

4.3.1 Intensity Variations

The range of trapping laser intensities covered is from 36-134 mW/cm^2. The trap laser detuning was varied from $133.5 - (52 * 2) \rightarrow 133.5 - (62 * 2)$ MHz which corresponds to $\delta/\Gamma = -4.9 \rightarrow -1.57$. The other MOT parameters are shown in the Table 4.1. In Fig. 4.6, the measured excited fraction is plotted as a function of saturation parameter s_0. As can be seen, most of the data lies within $0.1 \leq s_0 \leq 1.25$ shown by the vertical lines. It is clear

Parameter	Value	Units
B-Field Gradient	~ 12.45	Gauss/cm
MOT Temperature	130 ± 100	μK
Repump Intensity	3.26	mW/cm^2
A typical I-Balance	25.3: 36.1: 30.7	mW/cm^2
MOT Density	$\sim 10^8$	atoms/cm^3
Vacuum Pressure	10^{-10}	Torr

Table 4.1: These are the typical MOT characteristics and values of repump laser intensity, intensity balance in each pair of beams, and the B-field gradients for the intensity variation data. The intensity is varied from 36-134 mW/cm^2.

that the s_0 is no longer a useful parameter for $s_0 \geq 1.25$ where $f \neq f(s_0)$. This is the range where a nice cloud of trap atom can not be seen with the CCD camera.

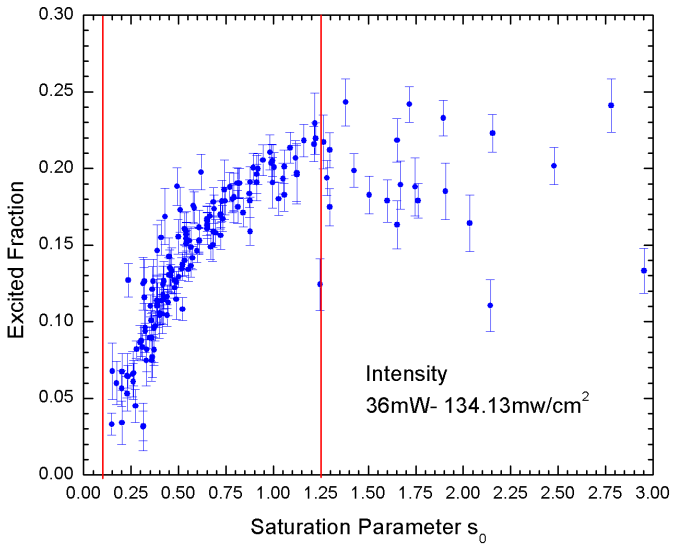

Figure 4.6: Measured excited fraction verses saturation parameter s_0. The detuning was varied from $\delta/\Gamma = -4.9 \rightarrow -1.57$ and the trapping laser intensity was varied from 36-134.13 mW/cm^2. To the right of vertical line at $s_0 = 1.25$, the MOT is extremely weak.

4.3.2 Intensity Balance

The excited fraction was also measured as a function of total trap laser intensities and detuning for a very different trap laser balance. The data for the new values of laser balance but with the other MOT parameters unchanged are shown in Fig. 4.7. In these data the intensities of the 3 pairs of counter propagating trap laser beams are 17.2, 30.2, 40.7 mW/cm^2.

balance.png

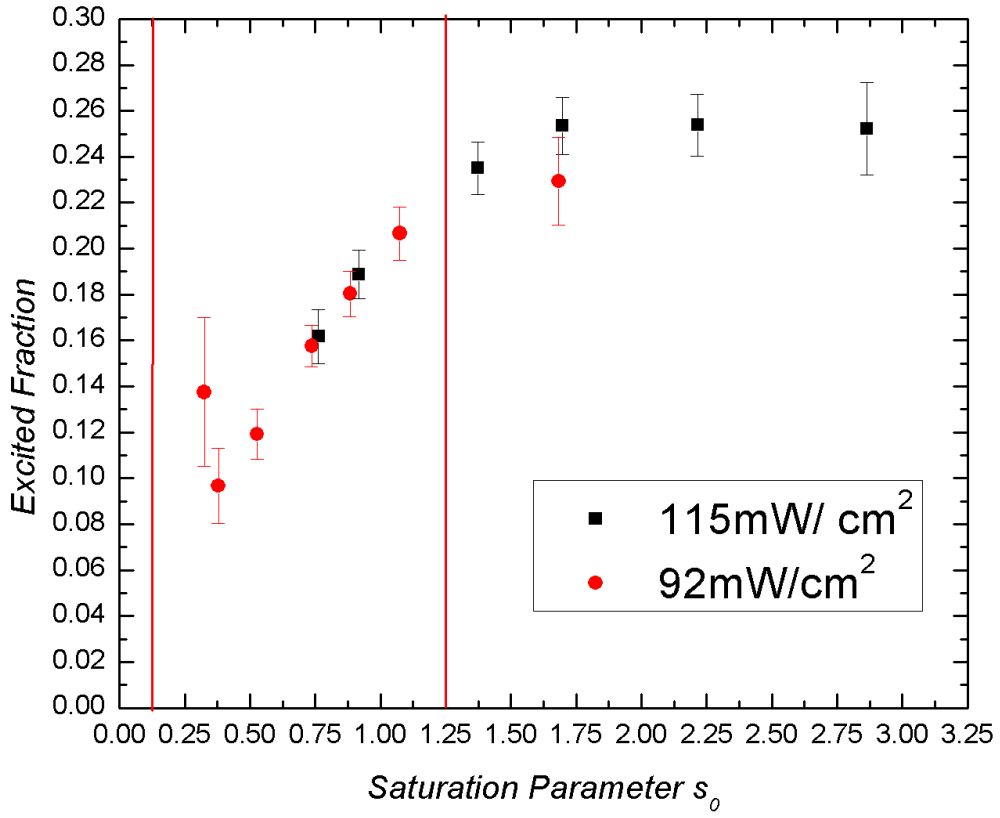

Figure 4.7: Excited fraction measurement when the balance in the beam's intensities is varied. The vertical lines are as in Fig. 4.6.

4.3.3 B-Field Gradient Effects

The results for the excited fraction as a function of saturation parameter s_0, for different value of B-field gradient are shown in the Fig. 4.8. The value of the gradient for the data is 7.66 G/cm, compared to 12.45 G/cm for the data of Figs. 4.6 and 4.7.

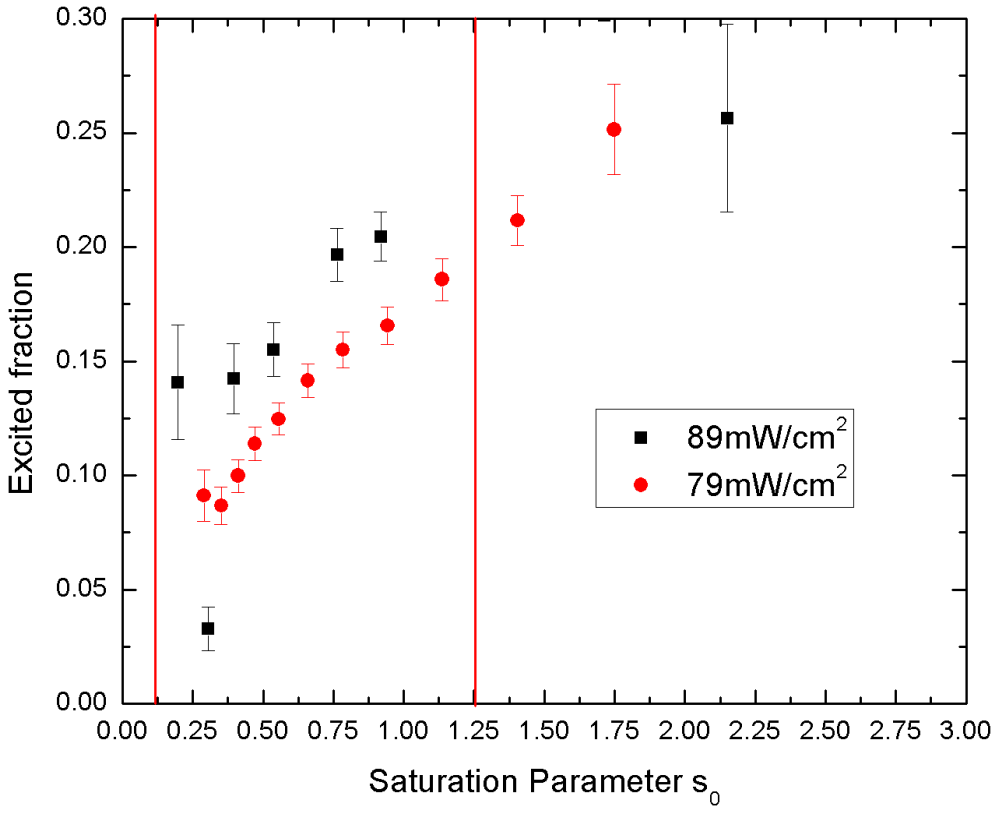

Figure 4.8: The B-field gradient is varied from the usual value of 12.45 G/cm to 7.66 G/cm. The excited fraction is measured as a function of saturation parameter s_0. The vertical lines are same as in Figs. 4.6

.

4.3.4 Repump Effects

In the following data the excited fraction was measured as a function of saturation intensity for various values of re-pump intensities and at value of detuning. All the data points are essentially lying on top of each other with the same excited fraction and error bars.

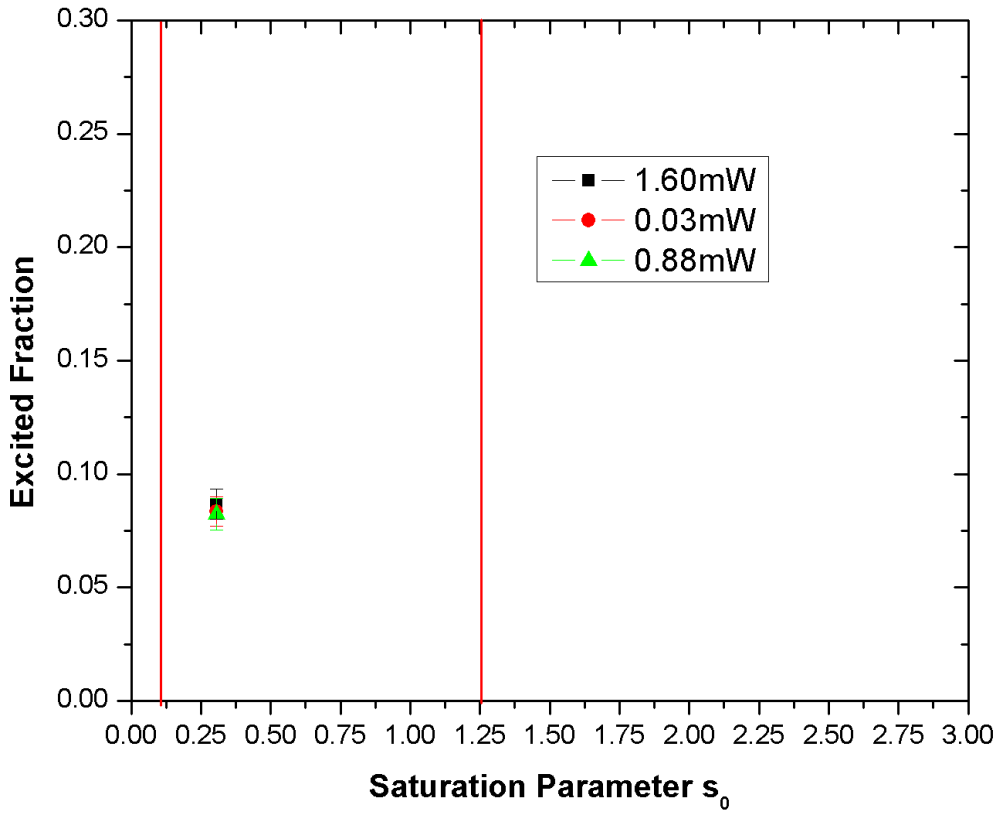

Figure 4.9: Excited fraction as a function of saturation parameter s_0 for various values of repump intensity, but for a fixed detuning. The vertical lines are same as in Fig. 4.6.

4.3.5 UCONN Data

In the UCONN work the photo-ionization rate of Rb(5p)in a MOT was measured as a function of trap laser intensity for several detunings [51]. They converted the measured rate to an excited fraction by assuming that the rate is directly proportional to f. The claim was that the scale for the excited fraction was set by assuming the at large intensity, the data would extrapolate to $f = 0.5$. However, this claim is difficult to understand, given the plots of Fig. 4.10. Following are their data for excited fraction as a function of intensity. Fig. 4.10 is the plot for excited fraction as a function of intensity for fixed detunings and Fig. 4.11 is

the plot for excited fraction as a function of saturation parameter s_0. It is obvious from the plot that the excited fraction is not tending to 50% for large intensity, as predicted by the simple model.

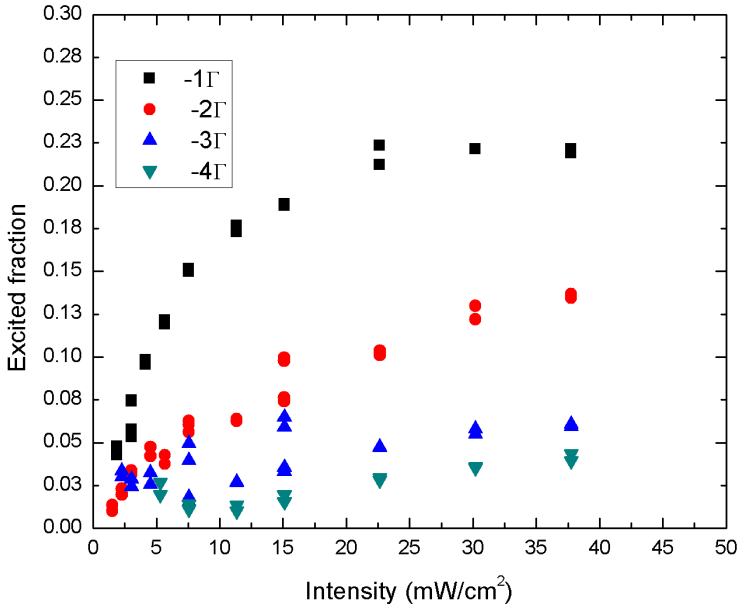

Figure 4.10: The plot of excited fraction as a function of intensity for various detunings. The detunings are colored-labelled for each data set.

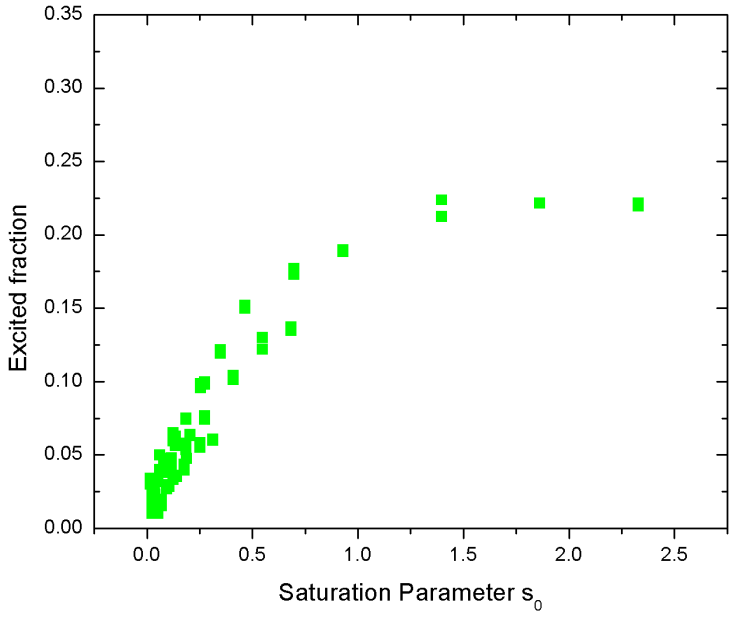

Figure 4.11: The plot of excited fraction as a function of saturation parameter s_0. The trends of the data can be seen clearly: the excited state is saturating at well below the limit predicted by the simple model.

4.3.6 All Results

Here all data, including the data from Gensemer[51] (labelled UCONN) are shown together. For one detuning they plotted this fraction as a function of intensity and used this in the simple model of section 2.1, using I_s as the free parameter. The green data points are the data from Gensemer[51]. Interestingly enough, their data match the data of the current measurements even though it is clear that the excited fraction saturates at a value for below their assumed value of $f_{max} = 0.5$. It seems most appropriate to plot the data as a function of the single variable s_0. However it may be of interest to see how f_m varies with δ and I. Therefore, the same data set for excited fraction for fixed detunings and various intensities are plotted in Appendix D.

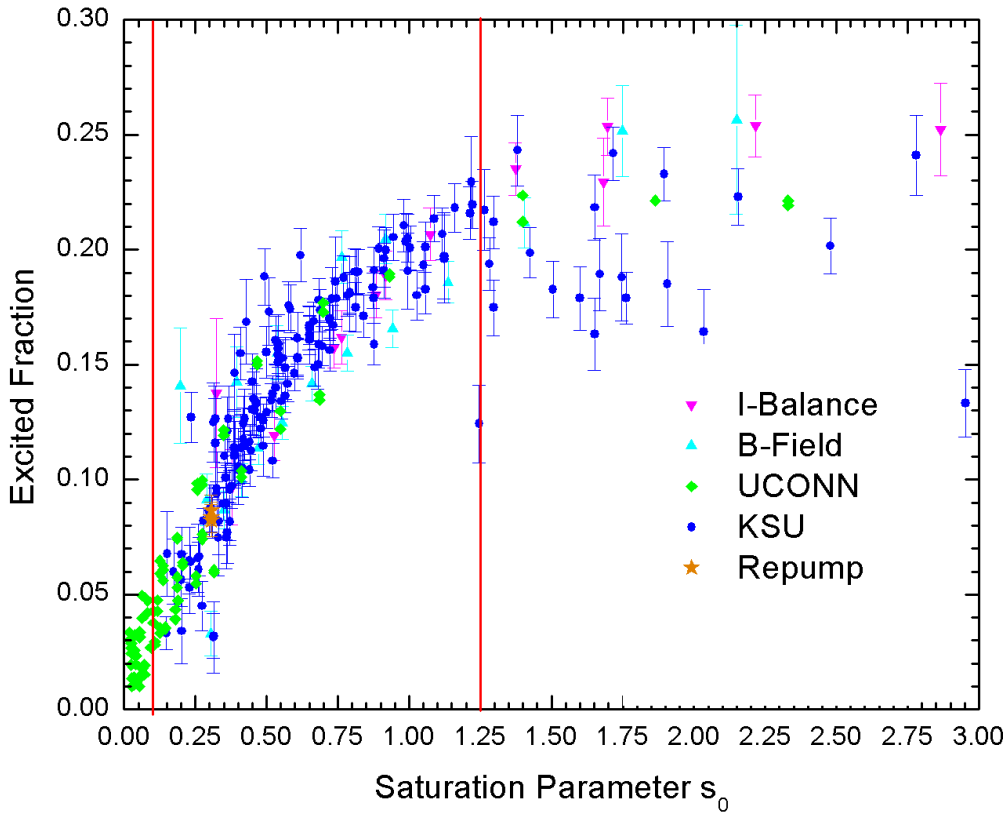

Figure 4.12: The plot of excited fraction for all data. The data include the results from the present experimental work along with the data for photo-ionization rates in Connecticut. The vertical line is as in Fig. 4.6.

4.4 Fitting Data

In order to test the validity of the theoretical models discussed in Chapter 2, the models must be fit to the data. In this section, we attempt to fit all these models to the data, and comment on the range of the validity of the models.

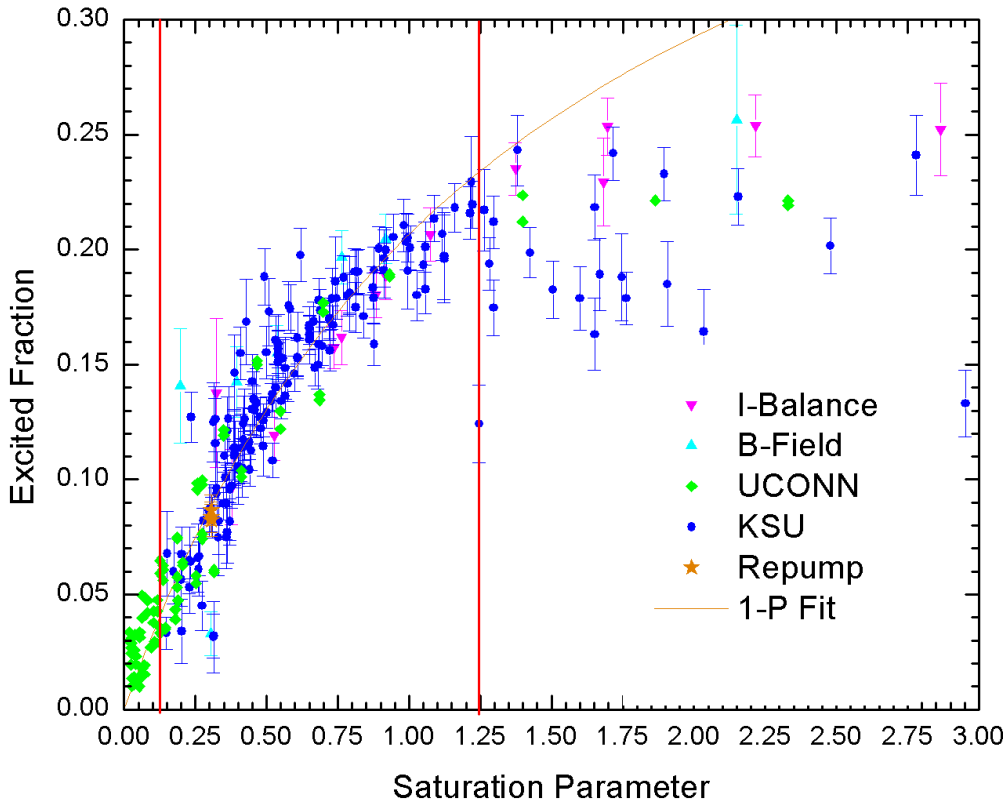

Figure 4.13: A one parameter model fit where $\tilde{I}_s$ is chosen as the free parameter.

4.4.1 Simple Model Fit

The simple two level model, referred to as the "1-parameter model", is given by

$$f_m = \frac{I/\tilde{I}_s}{1 + 2I/\tilde{I}_s + (2\delta/\Gamma)^2}, \tag{4.13}$$

where $\tilde{I}_s$ is the free parameter to be fit to the data colored blue (KSU).

As can be seen in Fig. 4.12, the model fit the data very well for $0.1 \leq s_0 \leq 1.25$. Outside that range there is a very little consistent dependence of f on s_0. The data appear to be scattered at $s_0 \geq 1.25$, but the data are reproducible so this scatter is due to physics. We choose to interpret the scatter as a total breakdown in the model. Note that f saturates

well below 0.5 unlike the prediction of the model. After fitting the model to the data within the specified range of $0.1 \leq s_0 \leq 1.25$, the saturation intensity was found to be $\tilde{I}_s = 9.2$ mW/cm^2.

4.4.2 Simple Model Residuals

The deviation of the data (KSU) from the simple model is plotted as a histogram plot for $0.1 \leq s_0 \leq 1.25$. The residuals were fit to a Gaussian, the width of the which is found to be about 2%. For example if the model predicts $f_m = 15\%$, the e^{-1} scatter of the data is from 14% to 16%. The data *seem* to exhibit much greater scatter than the histogram of Fig. 4.14 indicates. This is because so many of the data points lie right on top of each other. This shows the value of histogramming the residuals, since this "degenracy" can be seen in a quantitative fashion.

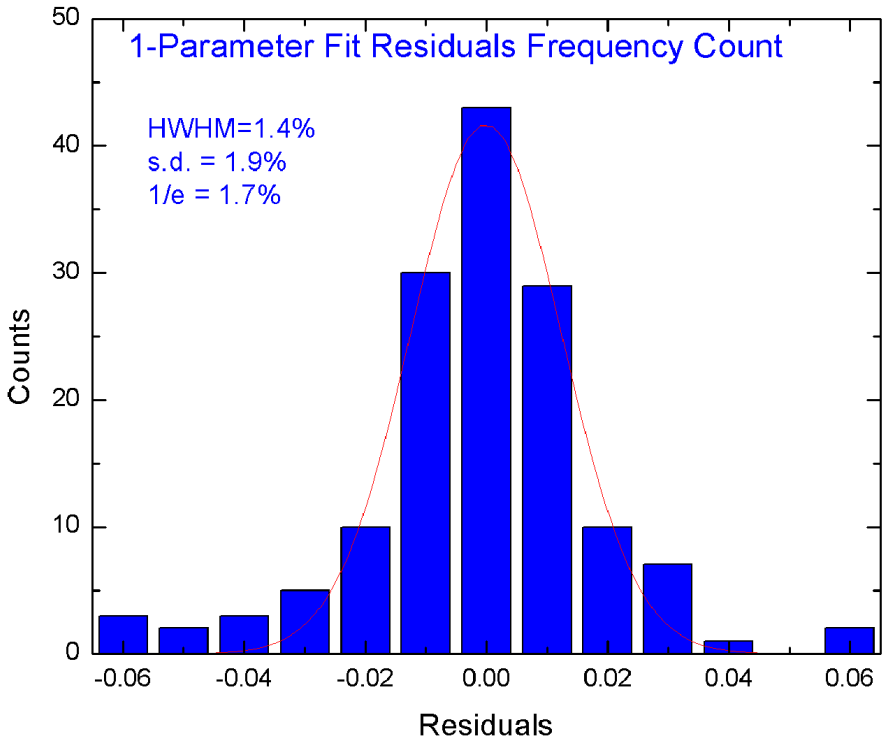

Figure 4.14: The residuals from the one parameter model are fit to a Gaussian with a FWHM at $1/e$ of 2%.

4.4.3 Error Bars on Saturation Intensity

From equation 4.13 the effective saturation intensity can be written as

$$\tilde{I}_s = \frac{I(1-2f_m)}{f_m[1+(2\delta/\Gamma)^2]}. \tag{4.14}$$

It is obvious from this equation that the $\tilde{I}_s$ depends on the three experimental quantities the excited fraction f_m, the total beam intensity I, and the trap laser detuning δ. In the calculation of error bars for $\tilde{I}_s$ all uncertainties in f_m, I, and δ are included using the following equation

$$\frac{\Delta I_s}{I_s} = \left\{ \left(\frac{1}{1-2f_m}\right)^2 \left(\frac{\Delta f_m}{f_m}\right)^2 + \left(\frac{\Delta p}{p}\right)^2 + 4\left(\frac{\Delta w}{w}\right)^2 + \left(\frac{8\delta/\Gamma}{1+(2\delta/\Gamma)^2}\right)^2 \left(\frac{\Delta\delta}{\Gamma}\right)^2 \right\}^{1/2} \tag{4.15}$$

here $\Delta p = 1.8mW$ and $\Delta w = 0.02$ are the uncertainties in the power and the beam spot size measurements, respectively, and $\Delta\delta = 1$ MHz is the uncertainty in our detuning from the resonance. The averaged over all values of f_m in the range $0.1 \leq s_0 \leq 1.25$, $\Delta f_m = 0.02$. This gives $\Delta I_s/I_s = 0.19$, or $\Delta I_s = 1.7$.

4.4.4 Modified Model Fit

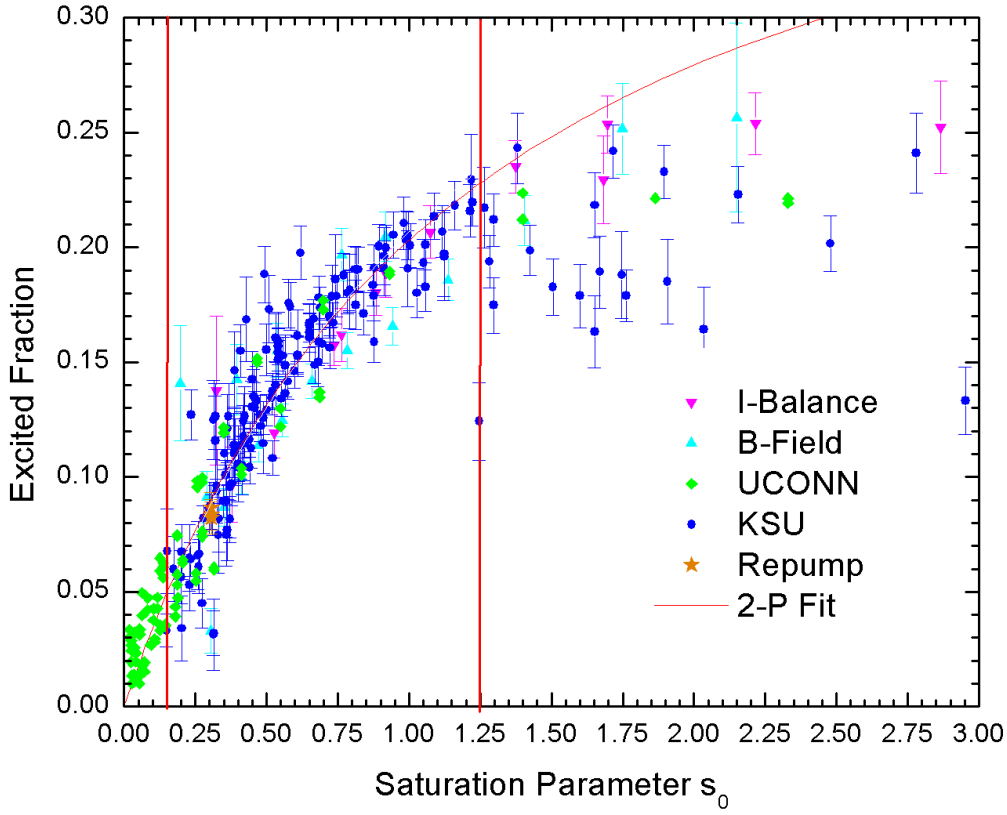

Figure 4.15: A two parameters model fit where C_1 and C_2 are chosen as the two parameters to be determined.

The modified model

$$f_m = \frac{C_1^2 I/I_s}{1 + C_2^2/I/I_s + (2\delta/\Gamma)^2} \tag{4.16}$$

was developed to hopefully better simulate a MOT-like configuration. We call it a two parameter model as there are two parameters C_1 and C_2 to be determined, as seen in Fig. 4.15. The 2-parameter model does fits the data (KSU) slightly better than the 1-parameter model within the range $0.1 \leq s_0 \leq 1.25$ model fits. The values extracted for C_1 and C_2 are $= 0.610$ and 0.645 respectively.

4.4.5 2-Parameter Residuals

The residuals of the 2-parameter fit for $0.1 \leq s_0 \leq 1.25$ are shown in Fig. 4.16. The histogram of residuals is virtually identical to that of the 1-parameter model.

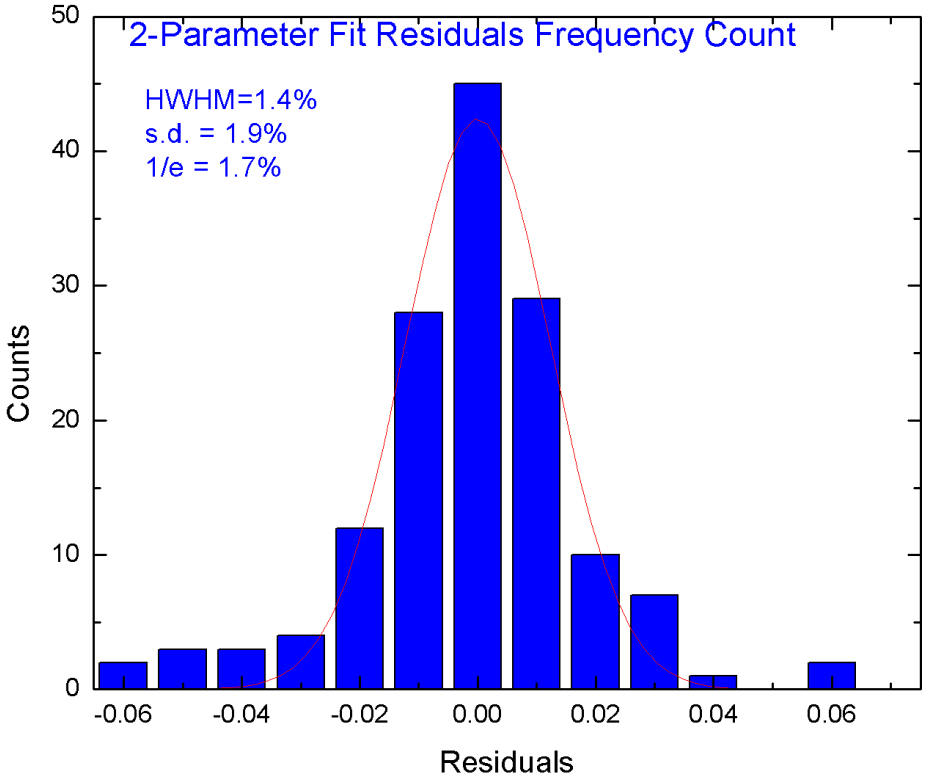

Figure 4.16: The residuals from the two parameter model are fit to a Gaussian with a FWHM as $1/e$ and of 2%.

4.4.6 Javanainen Model

The Javanainen model given by,

$$f = \frac{y}{1+2y}, \tag{4.17}$$

where

$$y = \left[\left(\frac{1}{\alpha} - \frac{1}{\beta}\right)\frac{s_r}{s+s_r} + \frac{1}{\beta}\right] s \tag{4.18}$$

has three parameters, α, β, and s_r to be fit to the data. The values calculated[20] for these parameters assuming random phases of trapping light for the D_2 cycling transition were $\alpha = 1.256$, $\beta = 1.620$, and $s_r = 1.045$. As we are not controlling the phases in our MOT we were expecting these parameters to be in more or less the same range as theory predicts. However what we found was that we could get *either* α *or* β to converge to a reasonable number but the other parameter and s_r were essentially indeterminant. This means that, in contrast to the basic premise of the model, there are no distinct " high" and "low" intensity regions in parameter space. We therefore are justified in rejecting this model out of hand.

4.5 Discussion

The set of all data including that of Gensemer[51], lies on a single well defined curve for $0.1 \leq s_0 \leq 1.25$. This strongly implies that the single parameter s_0 can be used to estimate the excited fraction in a MOT. Clearly the data cannot be made to fit such a simple function for $s > 1.25$. Perhaps this is because the 2-level approximations used in these models is less valid as the detuning from resonance is reduced. That is, when the detuning starts to become comparable to the Zeeman splitting, then the two level model completely breaks down.

One can see that for $s > 1.25$ the data seem to scatter with amplitudes greater than their assigned error bars. This is not due to an underestimation of uncertainty in measured excited state fraction because the data are reproducible within the error bars. Rather, the scattering is due to s ceasing to be a good parameter. Once again this is thought to be a breakdown of the simple two level model. It should be noted that values of s beyond about 1.25 correspond to a regime of MOT parameters space that is rarely frequented in experiments due to the extremely low number of trapped atoms that result.

The 1-and 2- parameter models discussed in Chapter 2, fit the data for $0.1 \leq s_0 \leq 1.25$. Both fits are very good over most of the interesting range. The 3-parameter model was found to be less satisfactory because the data show no indication of separate "high s_0" and "low s_0" regimes. Therefore, fitted values of either α or β tends toward infinity and s_r tends to be indeterminant. To within experimental scatter, nearly all the data lie on the "universal curves" of 1- and 2-parameter fits, even though the MOT fluorescence varies from very bright to barely visible. This implies that the cold collisions in the MOT, which go as the square of the density, do not cause the excited fraction to deviate from the simple model, at least over the range of MOT parameters studied here (for $0.1 \leq s_0 \leq 1.25$).

Histograms of the residual plots, for both models, were fit to Gaussians. It is clear

that, given the trapping laser detuning and intensity, and therefore s_0, one can estimate the excited state fraction in a ^{87}Rb MOT to within a couple of percent with a great deal of confidence.

Note that while the 2-parameter model does fit the data slightly better than the 1-parameter model, the residuals of the two models are very similar over the useful region of s_0. Thus, there seems to be no real advantage in going beyond the 1-parameter model. the best fit to this model yields a value of effective $\tilde{I}_s$ of 9.2 ± 1.70 mW/cm^2. A best fit of the 2-parameter model of the data gives values $C_1 = 0.610$ and $C_2 = 0.645$. For both models the uncertainty in the excited state fraction as indicated by the plotted residuals is about 2%.

Chapter 5

Conclusion and Outlook

This chapter concludes the dissertation and discusses future research in this area.

5.1 Conclusion

In conclusion, the goal of this dissertation was to test the existing models for excited fraction in many laser cooled atom experiments. The technique used is a powerful one which holds the promise of probing coherent excitation dynamics with high resolution in cold atoms. This technique provides a high-resolution measurement of each energy state involved in the collision process, and provides a dynamic, noninvasive method of measuring fractional populations in all resolvable capture channels. These measurements are model-independent and also show the robustness of the MOT excited fraction to the various experimental parameters. The excited fraction is shown to be a function of laser beam intensity and detuning and is measured for various values on those parameters. The detuning is varied from $\delta/\Gamma = -1.57 \rightarrow -4.9$ with intensity ranging from 36-134 mW/cm^2.

A new way of measuring the laser beam spot size with less uncertainty was introduced. The excited fraction data were compared with the models and were found to be in a good agreement over the range of MOT parameters typically used by the cold atom community. We hope that this project will serve the MOT community as a touchstone in their experimental investigations.

The final, most important result of this thesis is that one can use equation 4.13, with $\tilde{I}_s = 9.2 \pm 1.70$ mW/cm^2, and assuming that one has *perfect* knowledge of I and δ, the error in predicted excited fraction can be written as

$$\frac{\Delta f_{th}}{f_{th}} = (1 - 2f_{th})\frac{\Delta \tilde{I}_s}{\tilde{I}_s}, \tag{5.1}$$

where $\Delta \tilde{I}_s / \tilde{I}_s = 0.19$. For example , for a typical value of $f_{th} = 0.15$, one finds $\Delta f_{th} = 0.02$, in agreement with our histogram of residuals shown in Fig. 4.14.

The measurements made in this dissertation will help in measuring cross sections in cold atoms collision where excited fraction and total number densities are critical. The MOT community dealing with ^{87}Rb with known values of their intensities and detunings ought to be able to extract the excited fractions by using the results of this thesis. Similar measurements for other alkali metal atom MOTs would also be helpful, as they will allow users of other MOT systems to make similarly accurate estimates of excited fractions in their MOTs. Furthermore, if several systems having different values of f and $\tilde{I}_s$ are investigated, perhaps some systematic conclusion could be obtained in which $\tilde{I}_s / I_s$ may be predicted for arbitrary systems.

Bibliography

[1] M. H. Anderson, J. R. Ensher, M. R. Mathews, C. E. Wieman, and E. A. Cornell, Science. **269**, 198 (1995).

[2] P. L. Gould, P. D. Lett, P. S. Julienne, and W. D. Phillips, Phys. Rev. Lett. **60**, 788 (1988).

[3] J. Dalibard and C. Cohen-Tannoudji, J. Opt. Soc. Am. B **2**, 1707 (1985).

[4] P. S. Julienne, Phys. Rev. Lett. **61**, 698 (1988).

[5] P. S. Julienne and R. Heather, Phys. Rev. Lett. **67**, 2135 (1991).

[6] J. Weiner, V. Bagnato, S. Zilio, and P. Julienne, Rev. Mod. Phys. **71**, 1 (1999).

[7] S. Chu, Rev. Mod. Phys. **70**, 685 (1998).

[8] W. D. Phillips, Rev. Mod. Phys. **70**, 721 (1998).

[9] T. W. Hansch and A. L. Schalow, Opt. Commun. **13**, 68 (1975).

[10] E. L. Raab, M. G. Prentiss, A. E. Cable, S. Chu, and D. E. Pritchard, Phys. Rev. Lett. **59**, 2631 (1987).

[11] P. G. Molenaar, P. van der Straten, and H. G. M. Heideman, Phys. Rev. Lett. **77**, 1460 (1996).

[12] A. Fioretti et al., Phys. Rev. Lett. **80**, 4402 (1998).

[13] C. Gabbanini, A. Fioretti, D. Lucchesini, S. Gozzini, and O. Mazzoni, Phys. Rev. Lett. **84**, 2814 (2000).

[14] T. P. Dinneen, C. D. Wallace, K. Y. N. Tan, and P. L. Gould, Opt. Lett. **17**, 1706 (1992).

[15] U. Gaubatz, P. Rudecki, S. Schiemann, M. Külz, and K. Bergmann, Chem. Phys. Lett. **149**, 463 (1988).

[16] S. B. Nagel et al., Phys. Rev. Lett. **94**, 083004 (2005).

[17] C. G. Townsend, *Laser Cooling and Trapping of Atoms*, PhD thesis, Merton College, Oxford, Mochaelmas, 1995.

[18] W. Demtröder, *Laser Spectroscopy: Basic Concepts and Instrumentation*, Springer, 2002.

[19] C. G. Townsend et al., Phys. Rev. A **52**, 1423 (1995).

[20] J. Javanainen, J. Opt. Soc. Am. B **10**, 572 (1993).

[21] M. van der Poel, C. V. Nielsen, M. A. Gearba, and N. Andersen, Phys. Rev. Lett. **87**, 123201 (2001).

[22] J. W. Turkstra et al., Phys. Rev. Lett. **87**, 123202 (2001).

[23] X. Fléchard, H. Nguyen, E. Wells, I. Ben-Itzhak, and B. D. DePaola, Phys. Rev. Lett. **87** (2001).

[24] G. Veshapidze, M. L. Trachy, M. H. Shah, and B. D. DePaola, Appl. Opt. **45**, 8197 (2006).

[25] B. H. Bransden and C. J. Joachain, *Physics of Atoms and Molecules*, volume 2nd Ed., Prentice Hall, New York, 2003.

[26] D. J. Griffiths, *Introduction to Quantum Mechanics*, Prentice Hall, New Jersey, 1995.

[27] H. J. Metcalf and P. van der Straten, *Laser Cooling and Trapping*, Springer-Verlag, New York, 1999.

[28] E. L. Raab, M. Prentiss, A. Cable, S. Chu, and D. E. Pritchard, Phys. Rev. Lett. **59**, 2631 (1987).

[29] S. Chu and C. Wieman, J. Opt. Soc. Am. B **6**, 2020 (1989).

[30] C. Wieman, G. Flowers, and S. Gilbert, Am. J. Phys. **63**, 317 (1995).

[31] H. Metcalf, J. Opt. Soc. Am. B **6**, 2206 (1989).

[32] E. Hecht, *Optics*, volume Third edition., Addison Wesley Longman, Inc, 1998.

[33] H. A. Camp, *Measurement of Time Evolution of Coherent Excitation*, PhD thesis, Kansas State University, 2005.

[34] K. L. Corwin, Z. T. Lu, C. F. Hand, R. J. Epstein, and C. E. Wieman, Appl. Opt. **37**, 15 (1998).

[35] K. B. MacAdam, A. Steinbach, and C. Wieman, Am. J. Phys. **60**, 1098 (1992).

[36] W. Lu et al., Rev. Sci. Instrum. **67**, 3003 (1996).

[37] B. T. H. Varcoe et al., Meas. Sci. Technol. **11**, N111 (2000).

[38] T. Petelski, M. Fattori, G. Lamporesi, J. Stuhler, and G. M. Tino, Eur. Phys. J. D **22**, 279 (2003).

[39] G. Wąsik, W. Gawlik, J. Zachorowski, and W. Zawadzki, Appl. Phys. B **75**, 613 (2002).

[40] M. Abramowitz and I. A. Stegun, Handbook of mathematical functions, NBS, 1964, (299).

[41] N. G. Kingsbury, Lecture Notes on Digital Modulation, Dept. of Engineering, University of Cambridge, Cambridge, UK., 1995, (Web based-publication).

[42] R. Dörner et al., Phys. Rep. **330**, 95 (2000).

[43] H. Schmidt-Böcking, R. Dörner, and J. Ullrich, Europhys. News **33/6**, 210 (2002).

[44] J. Ullrich et al., Rep. Prog. Phys. **66**, 1463 (2003).

[45] V. Mergel et al., Nucl. Instrum. Methods Phys. Res., Sect. B **98**, 593 (1995).

[46] R. Brédy, H. Nguyen, H. A. Camp, X. Fléchard, and B. D. DePaola, Nucl. Instrum. Methods **205**, 191 (2003).

[47] H. Nguyen, X. Fléchard, R. Brédy, H. A. Camp, and B. D. DePaola, Rev. Sci. Instrum. **75**, 2638 (2004).

[48] In reality, a typical Wiley-McLaren spectrometer[52] could have been used, but the MOTRIMS spectrometer was originally designed for precision measurements of both Q-Value and scattering angle.

[49] H. Nguyen, *MOTRIMS*, PhD thesis, Kansas State University, 2003.

[50] T. G. Lee, H. Nguyen, X. Fléchard, B. D. DePaola, and C. D. Lin, Phys. Rev. A **66**, 042701 (2002).

[51] S. Gensemer, Private Communication, Unpublished., 2006.

[52] W. C. Wiley and I. H. McLaren, Rev. Sci. Instrum. **26**, 1150 (1955).

Appendix A

Electronic Circuit Diagrams

Most of the in-house electronic circuitry used for construction or control of the MOT and associated lasers has been published elsewhere.[49] Three new circuits, however, have been designed since these publications, and are included in this appendix. They are:

- **Peak Locking**

  Electronic diagram showing the latest peak locking circuitry.

- **Frequency Shifter**

  Electronic circuit diagram for shifting the AOM frequency.

- **AOM Controller**

  The AOM controller circuit diagram is shown, along with the external control hardware associated with the AOM.

A.1 Peak Locking

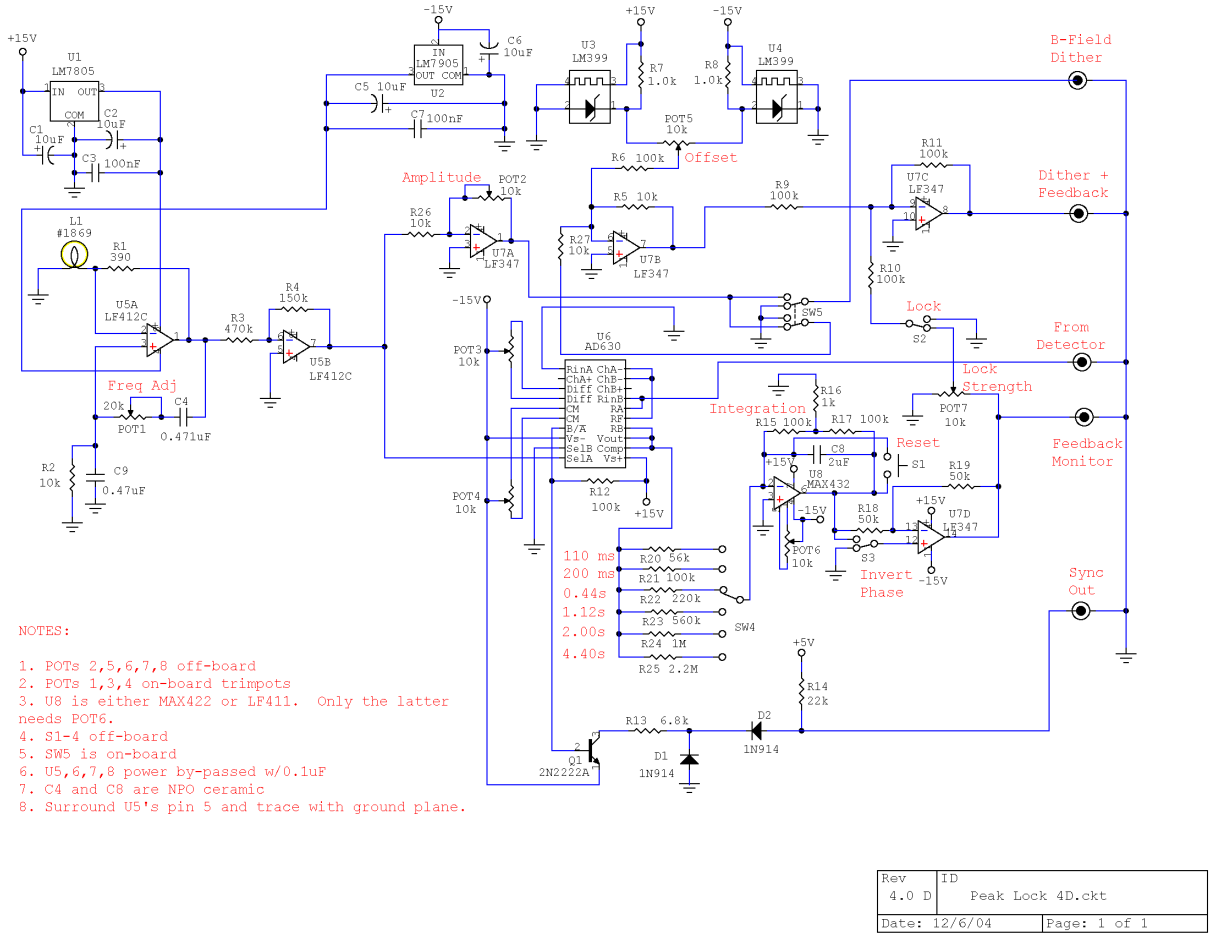

Figure A.1: Peak locking circuit diagram.

A.2 AOM Controller

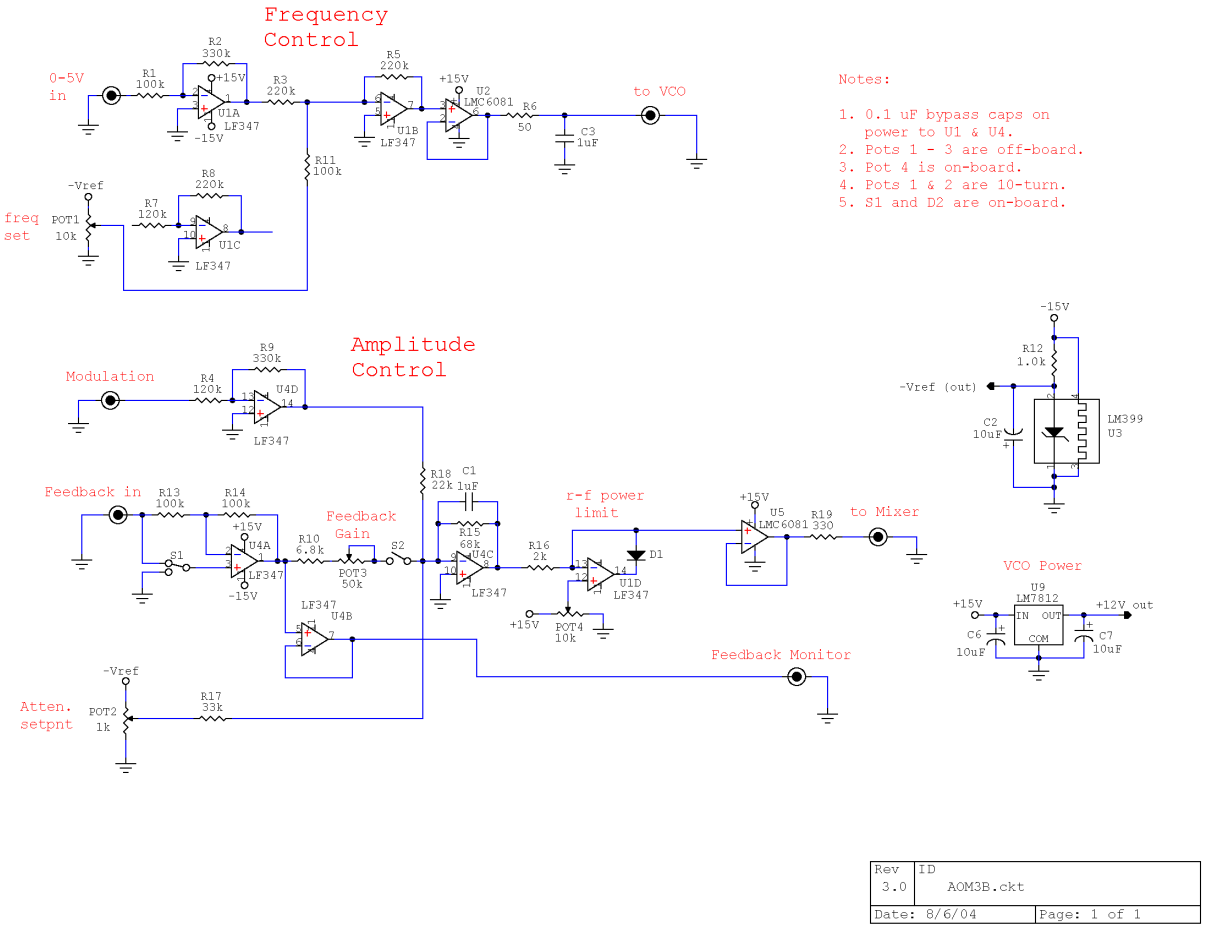

Figure A.2: AOM control circuit diagram.

The AOM controller circuitry allows one to control the amplitude and detuned frequency of the diffracted light passing through the AOM, and includes an RF switch to rapidly turn the AOM on or off. The control box houses the circuit described in Fig. A.2, which provides a quasi-DC voltage to the mixer, and supplies an operating voltage to the voltage control oscillator (VCO). The frequency control signal supplied by the control box is converted by the VCO into an oscillating voltage, which in turn is fed into the mixer. The mixer takes the VCO output and appropriately attenuates it depending on the value of the quasi-DC amplitude signal received from the control box. In this manner, the amplitude and frequency

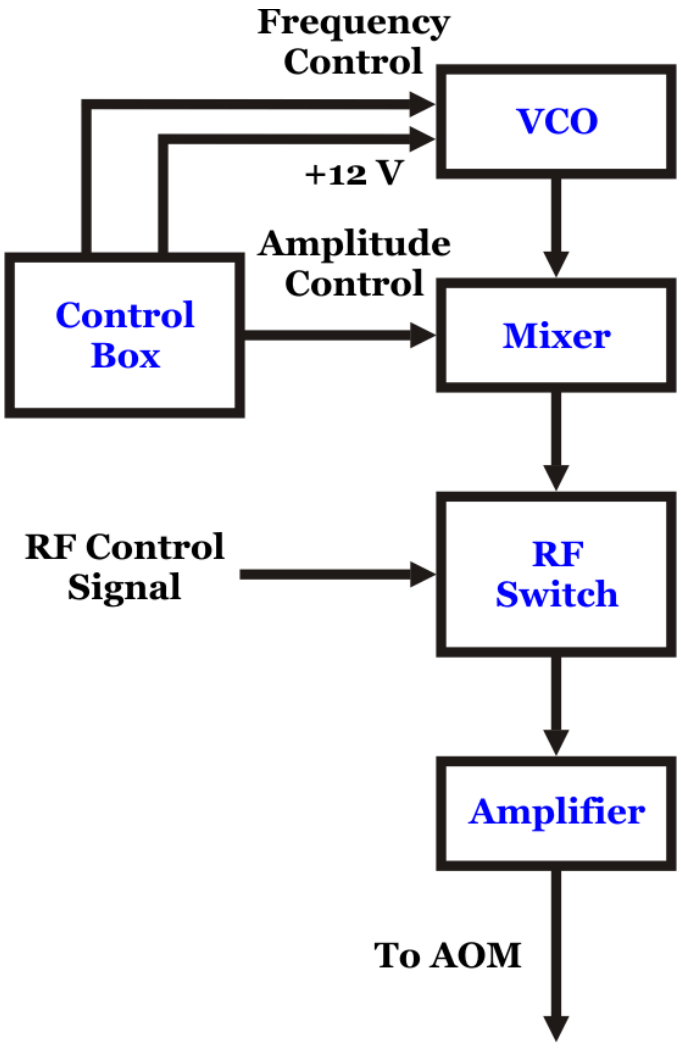

Figure A.3: Experimental setup for AOM control.

fed into the AOM are independently set by the controller box. The RF switch allows one to rapidly turn the signal on and off, while the amplifier places the signal in the proper operating range for the AOM.

A.3 Frequency Shifter

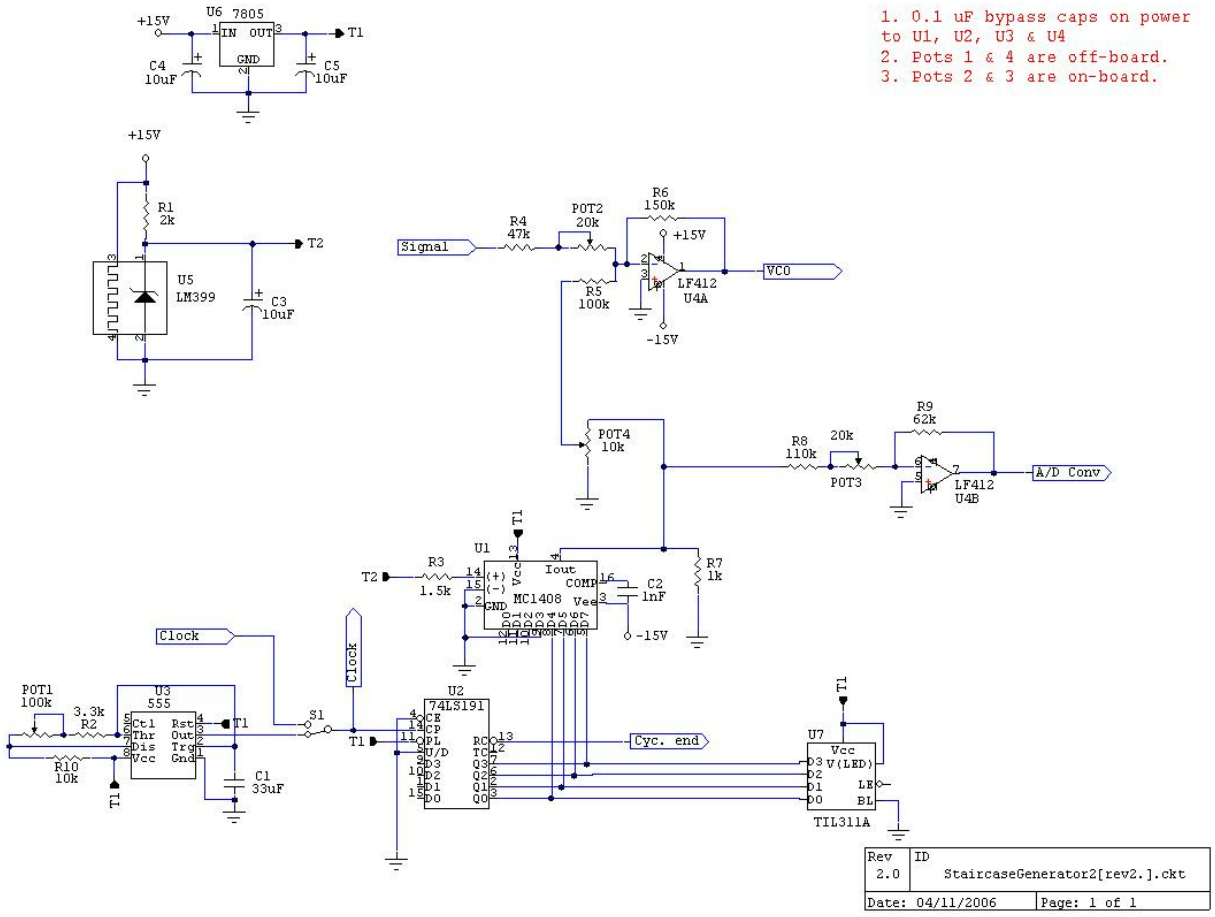

Figure A.4: Frequency shifter circuitry diagram.

Appendix B

RF Frequency Step vs Detuning

This is the table that corresponds to each RF frequency step from the frequency shifter and the corresponding detuning in terms of Γ.

Step Number	RF freq.(MHz)	Detuning(Γ)
0	52.09	-4.91137
1	52.73	-4.697324
2	53.36	-4.486622
3	54.01	-4.269231
4	54.66	-4.051839
5	55.31	-3.834448
6	55.97	-3.613712
7	56.63	-3.392977
8	57.30	-3.168896
9	57.97	-2.944816
10	58.64	-2.720736
11	59.32	-2.493311
12	60.01	-2.262542
13	60.69	-2.035117
14	61.38	-1.804348
15	62.06	-1.576923

Table B.1: RF frequency vs the laser detuning

Appendix C

Excited Fraction Scripts

The following scripts were used with Origin to determine the excited fraction in the $5p - 3p$ and $5s - 3s$ channels. The actual Origin notebook should be accessed if this code is intended to be run. The scripts included here are:

- **A Gaussian Fit Script** This script measures the excited fraction by fitting a Gaussian function to the peaks and calculates the error bars by error propagation method.
- **An Integration Fit Script**

  This script also measures the excited fraction but it measures area under the curve. It also calculates the error bars by the error propagation method.
- **Intensity Script**

  This script measures the peak intensity value and its width as well as the area under the peak.

C.1 A Gaussian Fit Script

The multifit parameter script allows one to run several hundred fits for a given data set automatically. The first few fits are checked by hand to make sure the range of background values allowed is appropriate, and then the program can be run as many times as one would like. The fit values, along with error bars, for each peak are stored in the indicated columns after each iteration.

```
/*
// +-----------------------------------------------------+
// |                                                     |
// |     Filename: detuning_analysis.txt                 |
// |                                                     |
// |  Description: Fit Gaussians to each both the ss and pp  |
// |          peaks in each of the detuning cuts in the      |
// |          Q-value vs detuning spectrum.              |
// |                                                     |
// |                                                     |
// +-----------------------------------------------------+

[MainSection]

// +-----------------------------------------------------+
// | Make sure the windows we want to create don't exist.    |
// +-----------------------------------------------------+
//window -cd TempDat;
//window -cd TempRaw;

for(j=1; j <= 15; j++) {
 create Det$(j) -w 100 Intensity ESF ESFErr Run;
 win -rl Det$(j) $(-%(DetuningList,2,j)) Gamma;
 worksheet -t 1 4;  // Make first column X
 worksheet -t 2 1;  // Make second column Y
// worksheet -t 3 3;  // Make third column Y Err
// worksheet -t 4 2;  // Ignore column 4
}
```

```
for(n=%(Params,4,1); n<=Params!wks.maxRows ; n++) {
 // If the file name is missing, skip the row.
 if("%(Params,1,n)" == (0/0)) { continue;};

// +--------------------------------------------------------+
 // | Create the worksheet to hold the results for this run
 // +--------------------------------------------------------+
create "Run%(Params,2,n)" -w 16 Detuning ESF ESFErr Intensity;
 worksheet -t 1 4;      // Make first column X
 worksheet -t 2 1;      // Make second column Y
// worksheet -t 3 3;    // This line isn't liked by Origin
                        // for some reason.
 // +--------------------------------------------------------+
 // | Read in the file locations for the data and store it   |
 // | in the variable A                                      |
 // +--------------------------------------------------------+

 %A = %(Params,1,n);

 // +--------------------------------------------------------+
 // | Create a new window, called TempRaw to hold the raw     |
 // | data. Import the ASCII file pointed to by A             |
 // +--------------------------------------------------------+

 window -n data TempRaw;
 open -w %A;
 window -r %H TempRaw;
```

```
// +-----------------------------------------------------+
// | Set columns 1, 2, 3 to be                           |
// | X, Y, and Z, respectively.                          |
// +-----------------------------------------------------+

Worksheet -t 1 4;
Worksheet -t 2 1;
Worksheet -t 3 6;

// +-------------------------------------------+
// | Select the Z (3rd) column                 |
// | Convert the raw data into a matrix        |
// | Rename the matrix window to TempMat       |
// +-------------------------------------------+

wks.colsel(3,1);
run.section(Wks,ConvReg);
Window -r %H TempMat;


// +-----------------------------------------------------+
// | Convert TempMat back into a worksheet called TempDat |
// +-----------------------------------------------------+

window -a TempMat;
matrix -t TempMat;
mat.matname$="TempMat";
win -n d TempDat;
mat.wksname$="TempDat";
mat.m2w();
window -r %H TempDat;

// +-----------------------------------------------------+
// | We no longer need the matrix. Kill it.              |
// +-----------------------------------------------------+

window -cd TempMat;
```

```
// +-----------------------------------------------------+
// | Create the worksheet to hold the working detuning step  |
// | Then set the first col to be row numbers (x) and the    |
// | second column to be y.                                  |
// +-----------------------------------------------------+


create FitData -w 256 A B;

loop  (i, 1, 256){%(FitData,1,i) = i;};
worksheet -t 1 4;
worksheet -t 2 1;




// +-----------------------------------------------+
// | Do the actual fitting.
// +-----------------------------------------------+

 // Populate FitData_B
copy %(TempDat,12) FitData_B;
a = peaks(FitData_B,4, 50);

 nlsf.func$ = Gauss;
nlsf.numReplica = 1;
nlsf.cleanUpFitData();
y0 = 0;
xc1 = a[2];
nlsf.v2 = 1; // Set xc1 to vary
A1 = %(FitData,2,a[2])*4;
w1 = 4;
nlsf.v3 = 1; // Set w1 to vary
```

```
xc2 = a[3];
nlsf.v5 = 1; // Set xc2 to be vary
A2 = %(FitData,2,a[3])*4;
w2 = 4;
nlsf.v6 = 1; // Set w2 to be vary

nlsf.fitdata$ = FitData_B;

nlsf.dataBegin = a[2]-10;
nlsf.dataEnd = 250;

nlsf.iterate(1000);
window -cd %H;




for (j=1; j <= 15; j++) {
 nlsf.func$ = Gauss;
 nlsf.numReplica = 1;
 nlsf.cleanUpFitData();
 y0 = 0;
 nlsf.v2 = 0; // Set xc1 to be fixed
 A1 = %(FitData,2,a[2])*4;
 nlsf.v3 = 0; // Set w1 to be fixed

 nlsf.v5 = 0; // Set xc2 to be fixed
 A2 = %(FitData,2,a[3])*4;
 nlsf.v6 = 0; // Set w2 to be fixed

 copy %(TempDat,j) FitData_B;
```

```
nlsf.fitdata$ = FitData_B;
nlsf.dataBegin = a[2] - 12;
nlsf.dataEnd =   250;
nlsf.simplex(1000);
nlsf.iterate(1000);

PP = nlsf.p4; // Parameter 4 is A1
SS = nlsf.p7; // Parameter 7 is A2
PPErr = nlsf.e4;
SSErr = nlsf.e7;

ESF = PP/(PP + SS*11.29);
ESFErrPP = PPErr*(1/(PP+SS*11.29)
          - PP/((PP+SS*11.29)*(PP+SS*11.29)));
ESFErrSS = SSErr*(PP/((PP+SS*11.29)
          *(PP+SS*11.29)))*11.29;
ESFErrR = 0.66*(PP/((PP+SS*11.29)
          *(PP+SS*11.29)))*SS;
ESFErr = sqrt(ESFErrPP*ESFErrPP
         + ESFErrSS*ESFErrSS + ESFErrR*ESFErrR);

if(%(Params,3,n) == (0/0)) {togroup=1; }
   % else {togroup=%(Params,3,n)};
if(togroup > 1) {togroup = togroup + 0.5;}
%D=Det$(j);
extracols = %D!wks.nCols - (togroup*2 + 1);
if (extracols < 0) {
  for (; extracols<0; extracols = extracols + 2) {
    %D!wks.addCol(ESF);
    %D!wks.col$(%D!wks.nCols).type=1;
    %D!wks.addCol(ESFErr);
    %D!wks.col$(%D!wks.nCols).type=3;
  }
}
%(Det$(j),1,n) = %(IntTable,n+1,j);
%(Det$(j),togroup*2,n) = ESF;
%(Det$(j),togroup*2+1,n) = ESFErr;
%(Det$(j),4,n) = %(Params,2,n);
%(Run%(Params,2,n),1,j) = %(DetuningList,2,j);
%(Run%(Params,2,n),2,j) = ESF;
%(Run%(Params,2,n),3,j) = ESFErr;
%(Run%(Params,2,n),4,j) = %(IntTable,n+1,j);
```

```
 // +-------------------------------------------------------+
  // | Destroy the extra windows we created                  |
  // +-------------------------------------------------------+

 window -cd %H;
 }
   window -cd TempDat;
   window -cd TempRaw;
   window -a Run%(Params,2,n);
   window -i;
}  window -cd TempDat; window -cd TempRaw;
   window -cd FitData;
   window -cd TempRaw;

for(j=1; j <= 15; j++) {
 win -a Det$(j);
 if (exist(GraphDet$(j)) != 0)
    { win -cd GraphDet$(j); };
 worksheet -s 2 0 wks.nCols 0;
 worksheet -p 201
 win -r %H GraphDet$(j);
 win -rl %H Graph $(-%(DetuningList,2,j)) Gamma;
 win -i;
 win -a Det$(j);
win -i;
}
```

C.2 Area Under the Curve Script

```
/*
// +-----------------------------------------------------------+
// |                                                           |
// |     Filename: detuning_analysis.txt                       |
// |                                                           |
// |  Description: Area under the curve fit to both the ss     |
// |                and pp peaks in each of the detuning       |
// |                cuts in the Q-value vs detuning spectrum.  |
// |                                                           |
// |                                                           |
// |                                                           |
// +-----------------------------------------------------------+



[MainSection]

// +-----------------------------------------------------------+
// | Make sure the windows we want to create don't exist.      |
// +-----------------------------------------------------------+
//window -cd TempDat;
//window -cd TempRaw;


for(j=1; j <= 15; j++) {
 create Det$(j) -w 100 Intensity ESF ESFErr Run;
 win -rl Det$(j) $(-%(DetuningList,2,j)) Gamma;
 worksheet -t 1 4;    // Make first column X
 worksheet -t 2 1;     // Make second column Y
// worksheet -t 3 3;    // Make third column Y Err
// worksheet -t 4 2;     // Ignore column 4
}
for(n=%(Params,4,1); n<=Params!wks.maxRows ; n++) {
            // If the file name is missing, skip the row.
 if("%(Params,1,n)" == (0/0)) { continue;};
```

```
// +-------------------------------------------------------+
 // | Create the worksheet to hold the results for this run   |
 // +-------------------------------------------------------+
create "Run%(Params,2,n)" -w 16 Detuning ESF ESFErr Intensity;
 worksheet -t 1 4;  // Make first column X
 worksheet -t 2 1;  // Make second column Y
// worksheet -t 3 3; // This line isn't liked by
                     //Origin for some reason.
 // +-------------------------------------------------------+
 // | Read in the file locations for the data and store it   |
 // | in the variable A                                      |
 // +-------------------------------------------------------+

 %A = %(Params,1,n);

 // +-------------------------------------------------------+
 // | Create a new window, called TempRaw to hold the raw     |
 // | data. Import the ASCII file pointed to by A             |
 // +-------------------------------------------------------+

 window -n data TempRaw;
 open -w %A;
 window -r %H TempRaw;
```

```
// +-------------------------------------------------------+
// | Set columns 1, 2, 3 to be                             |
// | X, Y, and Z, respectively.                            |
// +-------------------------------------------------------+

Worksheet -t 1 4;
Worksheet -t 2 1;
Worksheet -t 3 6;

// +-------------------------------------------------------+
// | Select the Z (3rd) column                             |
// | Convert the raw data into a matrix                    |
// | Rename the matrix window to TempMat                   |
// +-------------------------------------------------------+

wks.colsel(3,1);
run.section(Wks,ConvReg);
Window -r %H TempMat;
```

```
// +-------------------------------------------------------+
 // | Convert TempMat back into a worksheet called TempDat    |
 // +-------------------------------------------------------+

 window -a TempMat;
 matrix -t TempMat;
 mat.matname$="TempMat";
 win -n d TempDat;
 mat.wksname$="TempDat";
 mat.m2w();
 window -r %H TempDat;

 // +-------------------------------------------------------+
 // | We no longer need the matrix. Kill it.                  |
 // +-------------------------------------------------------+

 window -cd TempMat;

 // +-------------------------------------------------------+
 // | Create the worksheet to hold the working detuning step  |
 // | Then set the first col to be row numbers (x) and the    |
 // | second column to be y.                                  |
 // +-------------------------------------------------------+


 create FitData -w 256 A B;

 loop  (i, 1, 256){%(FitData,1,i) = i;};
 worksheet -t 1 4;
 worksheet -t 2 1;
```

```
// +---------------------------------------------+
 // | Do the actual fitting.
 // +---------------------------------------------+

  // Populate FitData_B
 copy %(TempDat,12) FitData_B;
 a = peaks(FitData_B,4, 50);

 min1 = FitData_B[a[1]];
 minchan1 = a[1];
 for (j=a[1]; j<a[2]; j++){
  if (min1 > FitData_B[j]) {
    min1 = FitData_B[j];
    minchan1 = j;
  }
 }

 min2 = FitData_B[a[2]];
 for (j=a[2]; j < a[3]; j++){
  if (min2 > FitData_B[j]) {
    min2 = FitData_B[j];
    minchan2 = j;
  }
 }

 startpp = minchan1;
 startss = minchan2;
 stopss = minchan2+2*(minchan2 - minchan1);

 for (j=1; j <= 15; j++) {
  copy %(TempDat,j) FitData_B;
  pp = 0;
  for (chan = startpp; chan < startss; chan++) {
    pp = pp + FitData_B[chan];
  }
  ss = 0;
  for (chan = startss; chan <= stopss; chan ++) {
    ss = ss + FitData_B[chan];
  }
```

```
PPErr = sqrt(pp);
SSErr = sqrt(ss);

background = 0;
for (chan=1;chan <= 25; chan++) {
  background = background + FitData_B[chan]
  + FitData_B[chan+225];
}
background = background / 100;
pp = pp - background * (startss - startpp);
ss = ss - background * (stopss - startss + 1);

ESF = PP/(PP + SS*11.29);
ESFErrPP = PPErr*(1/(PP+SS*11.29)
          - PP/((PP+SS*11.29)*(PP+SS*11.29)));
ESFErrSS = SSErr*(PP/((PP+SS*11.29)
           *(PP+SS*11.29)))*11.29;
ESFErrR = 0.66*(PP/((PP+SS*11.29)
          *(PP+SS*11.29)))*SS;
ESFErr = sqrt(ESFErrPP*ESFErrPP
         + ESFErrSS*ESFErrSS + ESFErrR*ESFErrR);
```

```
%(Det$(j),1,n) = %(IntTable,n+1,j);
  %(Det$(j),2,n) = ESF;
  %(Det$(j),3,n) = ESFErr;
  %(Det$(j),4,n) = %(Params,2,n);
  %(Run%(Params,2,n),1,j) = %(DetuningList,2,j);
  %(Run%(Params,2,n),2,j) = ESF;
  %(Run%(Params,2,n),3,j) = ESFErr;
  %(Run%(Params,2,n),4,j) = %(IntTable,n+1,j);
// +-----------------------------------------------+
  // | Destroy the extra windows we created
  // +-----------------------------------------------+

 }
   window -cd TempDat;
   window -cd TempRaw;
   window -a Run%(Params,2,n);
   window -i;
}  window -cd TempDat; window -cd TempRaw;
   window -cd FitData;
   window -cd TempRaw;
//for(j=1; j <= 15; j++) {
// win -a Det$(j);
// if (exist(GraphDet$(j)) != 0)
   { win -cd GraphDet$(j);};
// worksheet -s 2 0 wks.nCols 0;
// worksheet -p 201
// win -r %H GraphDet$(j);
// win -rl %H Graph $(-%(DetuningList,2,j)) Gamma;
// win -i;
// win -a Det$(j);
// win -i;
//}
```

C.3 Peak Intensity Fit

A Gaussian peak fit on the data for determination of peak intensity, and fluctuation in it.

```
// +-------------------------------------------------------+
// |                                                       |
// |     Filename: detuning_analysis.txt                   |
// |                                                       |
// |  Description: Fit Gaussians to each peak value        |
// |          corresponding to  each detuning in           |
// |          Intensity vs detuning spectrum.              |
// |                                                       |
// +-------------------------------------------------------+

[MainSection]

// +-------------------------------------------------------+
// | Make sure the windows we want to create don't exist.
// +-------------------------------------------------------+
window -cd TempDat;
// window -cd TempMat;
window -cd TempRaw;

// +-------------------------------------------------------+
// | Set the 'Filelist' worksheet to be the active worksheet
// +-------------------------------------------------------+

window -a Filelist;
for(n=1; %(FileList,1,n) != "--"; n=n+1) {
```

```
// +-----------------------------------------------------+
// | Read in the file locations for the data and store it |
// | in the variable A                                    |
// +-----------------------------------------------------+

%A = %(FileList,1,n);




// +-----------------------------------------------------+
// | Create a new window, called TempRaw to hold the raw  |
// | data. Import the ASCII file pointed to by A          |
// +-----------------------------------------------------+

window -n data TempRaw;
open -w %A;
window -r %H TempRaw;

// +-----------------------------------------------------+
// | Set columns 1, 2, 3 to be                            |
// | X, Y, and Z, respectively.                           |
// +-----------------------------------------------------+

Worksheet -t 1 4;
Worksheet -t 2 1;
Worksheet -t 3 6;
```

```
// +-------------------------------------------------------+
// | Select the Z (3rd) column                             |
// | Convert the raw data into a matrix                    |
// | Rename the matrix window to TempMat                   |
// +-------------------------------------------------------+

wks.colsel(3,1);
run.section(Wks,ConvReg);
Window -r %H TempMat;

// +-------------------------------------------------------+
// | Convert TempMat back into a worksheet called TempDat
// +-------------------------------------------------------+

window -a TempMat;
mat.matname$="TempMat";
win -n d TempDat;
mat.wksname$="TempDat";
mat.m2w();
window -r %H TempDat;




// +-------------------------------------------------------+
// | We no longer need the matrix. Kill it.
// +-------------------------------------------------------+

window -cd TempMat;
```

```
// +-----------------------------------------------------+
// | Create the worksheet to hold the results for this run
// +-----------------------------------------------------+
create %(Filelist,2,n) -w 16 detuning xc xerr w wErr A Aerr;
worksheet -t 1 4;
worksheet -t 2 1;
worksheet -t 3 3;
worksheet -t 4 1;
worksheet -t 5 3;
worksheet -t 6 1;
worksheet -t 7 3;

// +-----------------------------------------------------+
// | Create the worksheet to hold the working detuning step
// | Then set the first col to be row numbers (x) and the
// | second column to be y.
// +-----------------------------------------------------+


create FitData -w 256 A B;

loop  (i, 1, 256){%(FitData,1,i) = i;};
worksheet -t 1 4;
worksheet -t 2 1;
// +-----------------------------------------------+
// | Do the actual fitting.
// +-----------------------------------------------+



for(j=1; j <= 15 ; j++) {
 // +-------------------------------------------------+
 // | Find the maximum point in this column
 // +-------------------------------------------------+
 FitData_B = %(TempDat,j);
 maxrow = 0;
 maxval = 0;
 loop (r, 1, 256) {
  if(FitData_B[r] > maxval) {
   maxval = FitData_B[r];
   maxrow = r;
  }
```

```
  }
  nlsf.func$ = Gauss;
  nlsf.cleanUpFitData();
  y0 = 0;
  xc = maxrow;
  A = 1000;
  w = 5;
  nlsf.fitdata$ = FitData_B;
  nlsf.iterate(100);
  %(%(FileList,2,n),1,j) = j;
  %(%(FileList,2,n),2,j) = nlsf.p2; // Parameter 2 is xc
  %(%(FileList,2,n),3,j) = nlsf.e2;
  %(%(FileList,2,n),4,j) = nlsf.p3; // Parameter 3 is w
  %(%(FileList,2,n),5,j) = nlsf.e3;
  %(%(FileList,2,n),6,j) = nlsf.p4; // Parameter 4 is A
  %(%(FileList,2,n),7,j) = nlsf.e4;
  // +--------------------------------------------+
  // | Destroy the extra windows we created
  // +--------------------------------------------+

 window -cd %H;
 }
// window -a %(FileList,2,n);
 window -cd TempDat;
 window -cd TempRaw;
 window -cd FitData;
}
```

Appendix D

Excited Fraction Data.

This is a plot of the excited fraction as a function of intensity for various detunings. Each colored data set represents the excited fraction for one detuning. It is difficult to get any physics out of this plot as there is no pattern to be seen.

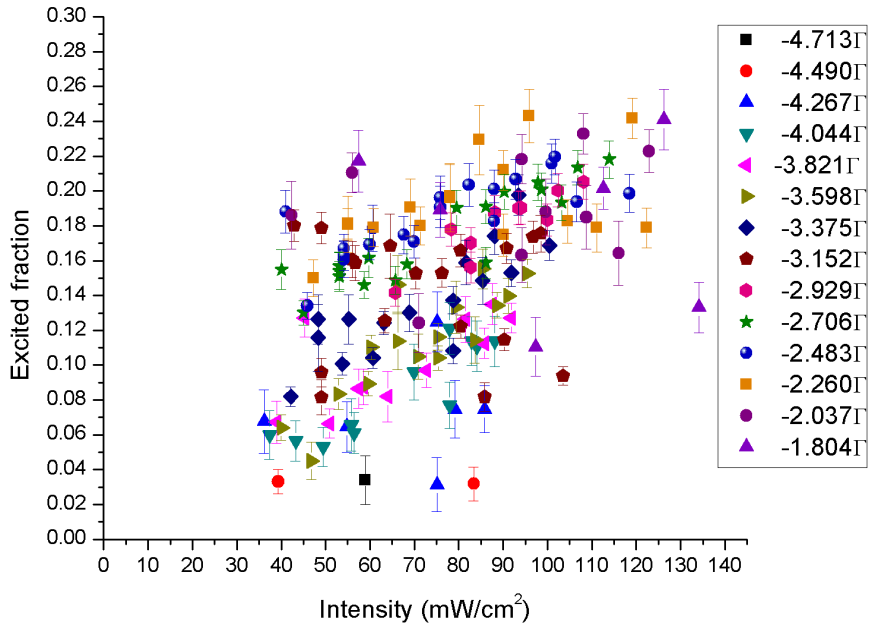

Figure D.1: The data for excited fraction is plotted as a function of Intensity.

Fig. D.2 is the same plot as in Fig D.1 but with each block representing one detuning. The detuning for each block is indicated in units of Γ. The intensity on the x-axis for each

block ranges from 30-130 mW/cm^2 except for detuning (-1.804) where the range is set to be 30-145mW/cm^2. Each minor tic corresponds to 10mW/cm^2. By putting each data set side by side we, finally, start to see a pattern like a "saw tooth". In this plot the data were first sorted by trap laser intensity, and then by detuning. As can be seen on lower detunings and high intensities the error bars start to increase which is due to the fact that the areas under the peaks in A_P and A_s are just hard to measure. The middle frequencies are the frequencies where the MOT community traps their atoms usually.

In order to see the universal feature of the data and common physics for each data set it was found best to plot the data in terms of saturation parameter s_0. Fig. D.3 is a plot of excited fraction as a function of s_0. The data set is the same as in Fig. 4.6, but for each

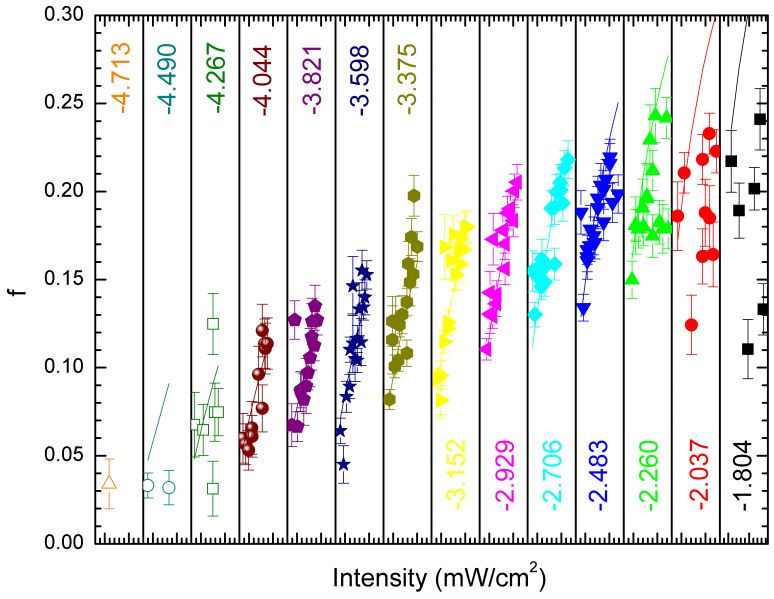

Figure D.2: The data for excited fraction is plotted as a function of Intensity.

detuning the data are sorted and plotted as colored data points. Each color represents a particular detuning and is labelled accordingly.

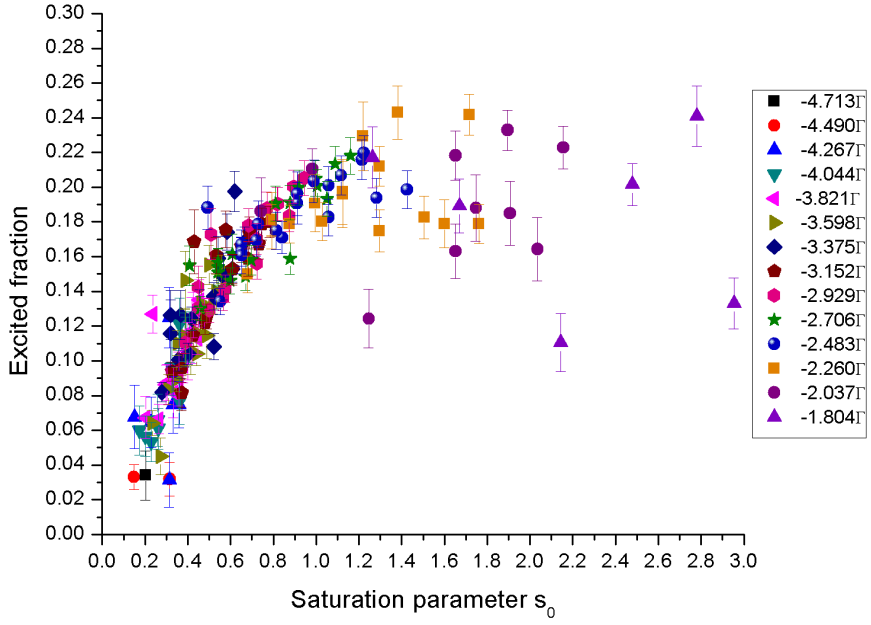

Figure D.3: The data for excited fraction is plotted as a function of saturation parameter s_0.